

Variational Assimilation of Global Microwave Rainfall Retrievals: Physical and Dynamical Impact on GEOS Analyses and Forecasts

Xin Lin¹, Sara Q. Zhang², and Arthur Y. Hou

Global Modeling and Assimilation Office

NASA Goddard Space Flight Center

Greenbelt, MD 20771

March 20, 2006

For submission to *Mon. Wea. Rev.*

Corresponding author's address:

Dr. Xin Lin

Global Modeling and Assimilation Office

NASA Goddard Space Flight Center, Code 610.1

Greenbelt, MD 20771

Email: xlin@gmao.gsfc.nasa.gov

¹ Additional affiliation: Goddard Earth Sciences & Technology Center, University of Maryland, Baltimore County, Baltimore, Maryland

² Additional affiliation: Science Applications International Corp., Beltsville, Maryland

Abstract

Global microwave rainfall retrievals from a 5-satellite constellation, including TMI from TRMM, SSM/I from DMSP F13, F14 and F15, and AMSR-E from EOS-AQUA, are assimilated into the NASA Goddard Earth Observing System (GEOS) Data Assimilation System (DAS) using a 1-D variational continuous assimilation (VCA) algorithm. The physical and dynamical impact of rainfall assimilation on GEOS analyses and forecasts is examined at various temporal and spatial scales.

This study demonstrates that the 1-D VCA algorithm, which was originally developed and evaluated for rainfall assimilations over tropical oceans, can effectively assimilate satellite microwave rainfall retrievals and improve GEOS analyses over both the Tropics and the extratropics where the atmospheric processes are dominated by different large-scale dynamics and moist physics, and also over the land, where rainfall estimates from passive microwave radiometers are believed to be less accurate.

Results show that rainfall assimilation renders the GEOS analysis physically and dynamically more consistent with the observed precipitation at the monthly-mean and 6-hour time scales. Over regions where the model precipitation tends to misbehave in distinctly different rainy regimes, the 1-D VCA algorithm, by compensating for errors in the model's moist time-tendency in a 6-h analysis window, is able to bring the rainfall analysis closer to the observed. The radiation and cloud fields also tend to be in better agreement with independent satellite observations in the rainfall-assimilation run especially over regions where rainfall analyses indicate large improvements.

Assimilation experiments with and without rainfall data for a midlatitude frontal system clearly indicates that the GEOS analysis is improved through changes in the thermodynamic and dynamic fields that respond to the rainfall assimilation. The synoptic structures of temperature, moisture, winds, divergence, and vertical motion, as well as vorticity are more realistically captured across the front. Short-term forecasts using initial conditions assimilated with rainfall data also show slight improvements.

1. Introduction

Global analyses as their quality continues to improve can be an important resource for analyzing multi-scale variability of the global hydrologic cycle and radiative energy budgets. By assimilating available observations into numerical weather prediction (NWP) models, it is possible to not only improve initial conditions for short-range forecasts but also gain useful information about model deficiencies. In the past decades space-borne measurements have been able to provide increasingly better global coverage and temporal sampling. Satellite observations of surface rainfall, vertical heating profiles, and cloud distributions are among a few most important variables that directly link to global water and energy cycle and the model's moist physics. Assimilating these new types of satellite observations into NWP models has become a challenge task. Although there are still significant uncertainties in these remotely-sensed measurements, tremendous effort has been expended to assimilate rainfall retrievals and/or rain-affected radiance as a first step to use satellite observation on precipitating/cloud processes to improve forecasts of severe weather events and short-term climate changes (e.g., Chang and Holt 1994, Zupanski and Mesinger 1995, Zou and Kuo 1996, Tsuyuki 1996a, b, 1997, Treadon 1997, Fillion and Errico 1997, Xiao et al. 2000, Macpherson 2001, Hou et al. 2000a, b, Krishnamurti et al. 2000a, b, Hou et al. 2001, Pu et al. 2002, Fillion 2002, Marecal and Mahfouf 2002, Marecal et al. 2002, Hou et al. 2004, Moreau et al. 2004, Pu and Tao 2004, Andersson et al. 2005, etc).

In recent years, variational algorithms have been the method of choice in global and regional weather forecast systems to assimilate satellite rainfall observations (e.g., Zupanski and Mesinger 1995, Tsuyuki 1996a, b, 1997, Hou et al. 2000a, b, Xiao et al. 2000, Marecal and Mahfouf 2000, Hou et al. 2001, Pu et al. 2002, Marecal et al. 2002, Marecal et al. 2002, Hou et al. 2004, Moreau et al. 2004, Pu and Tao 2004, Andersson et al. 2005). For example, by modifying the convective parameterization and substantially reducing the discontinuities in the treatment of the moist processes, Zupanski and Mesinger (1995) examined the benefit of assimilating precipitation data, and showed a fast convergence of their minimization process and an improvement of the precipitation forecast in midlatitudes. By assimilating rainfall information in a mesoscale model to get a better control of initial and lateral boundary conditions, Zou and Kuo (1996) demonstrated that the locations and intensities of many observed mesoscale features

can be better captured comparing with the one with conventional initialization procedures. Tsuyuki (1996a, 1996b, 1997) investigated the performance of a 4-DVAR technique in the Tropics by assimilating satellite-derived precipitation rates. His results indicated positive impacts on the tropical analyses of divergence, moisture and lower-troposphere vorticity, as well as precipitation forecasts. The European Center for Medium-Range Weather Forecasts (ECMWF) evaluated different variational assimilation techniques on rainfall retrievals ranging from 1-DVAR, to 4-DVAR, as well as direct assimilation of rain-affected radiance (e.g., Marecal and Mahfouf 2000, Marecal and Mahfouf 2002, Marecal et al. 2002, Marecal and Mahfouf 2003, Moreau et al. 2002, Andersson et al. 2005), and all of these approaches showed promising improvements on the analyzed and forecasted dynamic and thermodynamic fields in tropical cyclones and midlatitude weather systems.

One assumption commonly used in many variational assimilation studies is that the model dynamics and physics are perfect, and the error in the initial condition is dominant. If the error in the initial condition can be minimized, a good forecast can then be achieved. Many 4-DVAR studies using satellite rainfall observations adopt the perfect model assumption to minimize errors in the initial condition, and have demonstrated improved forecasts and analyses. A tangent linear model is usually introduced to describe the time evolution of the perturbation solution linearized around the basic state of a full nonlinear trajectory. As pointed out by Marecal and Mahfouf (2003), the model physics especially for the convection and microphysics parameterizations which are vital to rainfall and cloud assimilations, however, may contain many highly nonlinear processes and discontinuities which are typically characterized by on/off processes. Considering that model physical parameterizations are numerical approximations to nature with many empirical formula and assumptions, simplifying these complicated physical parameterizations so that they can be linearized for use in the adjoint model will certainly make the model physics further imperfect. Such problems, if not carefully controlled, could often lead to large departure of the model-predicted rain rate from the observed and severely limit the effective utilization of available satellite observations.

In addressing some of the concerns with assimilating rainfall data using the perfect model assumption, Hou et al. (2000a, b, 2001, 2004) developed a 1-D variational continuous

assimilation (VCA; Derber 1989) algorithm for assimilating tropical rainfall data using the model as a weak constraint. The scheme employs a precipitation observation operator based on a 6-h integration of a column model of moist physics along with prescribed large-scale forcing from the full model, and use moisture/temperature time-tendency corrections as the control variables to offset model deficiencies. The tendency corrections due to the rainfall assimilation are in addition to those due to the conventional data assimilation, and the error in the model moist physics is considered dominant. Such a methodology, by using satellite rainfall observations to compensate for the error in the model state variables, provides a useful way to identify deficiencies in the model moist physics. Their results have shown that the 1D VCA scheme is effective for assimilating rainfall data in the Tropics, where the model precipitation is known to be sensitive to parameterized moist physics in a vertical column. Along with improved rainfall analyses and forecasts, the monthly statistics of radiative fluxes, clouds, and total precipitable water (TPW) are in better agreement with independent satellite observations.

The extent to which global analysis and forecast can be improved depends not only on the assimilation method but also on the temporal sampling and spatial coverage of observations. The Global Precipitation Measurement (GPM) mission being planned for the beginning of the next decade is based on the concept of providing frequent global precipitation measurements using a space-borne precipitation radar as a calibrator of a constellation of passive microwave radiometers. GPM is designed to extend the successful Tropical Rainfall Measurement Mission (TRMM) in the tropics to higher latitudes, but with better temporal sampling and more accurate precipitation measurements. As a precursor to GPM, this study examines the impact of assimilating microwave rainfall retrievals from the current fleet of 5 satellites using the 1-D VCA methodology developed by Hou et al. (2000a, 2004). We will evaluate the impact of assimilating 6h rain accumulation on global analyses produced by the Goddard Earth Observing System (GEOS) in both the Tropics and the extratropics. Particular attention will be paid to the effectiveness of the 1-D VCA scheme for rainfall assimilation outside the Tropics, where atmospheric processes are governed by multivariate quasi-geostrophic dynamics and large-scale condensational precipitation. We will investigate the impact of rainfall assimilation on analyses in different climate regimes at several temporal and spatial scales.

The paper is organized as follows: section 2 introduces the microwave rainfall retrievals from various satellites and data preparations for assimilating into the model. Section 3 briefly describes the 1D VCA developed by Hou et al. (2000a, 2004) and the NASA GEOS3 system. Sections 4 and 5 evaluate the physical and dynamical impact of the rainfall assimilation on the GEOS system at monthly time scales, and selected climate regimes at 6-hourly time scales. Section 6 examines the impact of rainfall assimilation on analysis and forecast of a midlatitude frontal system. Section 7 gives a summary and conclusions.

2. Satellite precipitation data

2a. Satellites and sensors

Data from a five-satellite constellation including the TRMM, Defense Meteorological Satellite Program (DMSP) F13, F14 and F15, and Earth Observing System (EOS) Aqua (formerly named as EOS-PM to signify its afternoon equatorial crossing time), are used in this study. Detailed information regarding the satellites and sensors is listed in Table 1.

The Special Sensor Microwave Imager (SSM/I) is one of a suite of sensors flown on the DMSP satellites. SSM/I is a seven-channel, four-frequency, linearly-polarized, passive microwave radiometric system that measures upwelling microwave radiance at 19.35, 22.235, 37.0, and 85.5 GHz. The DMSP satellite orbits are near circular and sun-synchronous, with an altitude of 860 km and an inclination of 98.8°. These satellites cross the equator at fixed local times, and have daylight equatorial crossing times of 6:16, 8:20, and 9:27 Local Time, respectively.

The TRMM satellite was launched in November 1997 to determine the temporal and spatial distributions of precipitation and latent heating in the Tropics and subtropics (Simpson et al. 1988, Kummerow et al. 1998). TRMM's orbit is circular, with an inclination angle of 35° relative to the equator. The satellite visits a given area at low latitudes about once per day, but at a different local time every day. The TRMM Microwave Imager (TMI: Kummerow et al. 1998) is a multi-channel passive microwave radiometer measuring radiances at five frequencies: 10.7, 19.4, 21.3, 37, and 85.5 GHz.

The Advanced Microwave Scanning Radiometer-EOS (AMSR-E) is one of the six sensors aboard Aqua, which flies in a sun-synchronous orbit with a daylight crossing time of 13:30 Local Time. It is a passive microwave radiometer, measuring brightness temperatures at 12 channels and 6 frequencies ranging from 6.9 to 89.0 GHz.

2b. Rainfall Retrievals

The microwave rainfall retrievals from TMI, SSM/I, and AMSR-E are combined in this study to provide better temporal and spatial coverage in both the Tropics and midlatitudes. The rainfall retrievals used here are all based on the most recent version of the NASA Goddard Profiling (GPROF) algorithm (Kummerow et al. 2001; Olson et al 2005). Over the ocean, the microwave frequencies can probe through smaller cloud particles to measure the microwave emission from the larger raindrops. Over land, the sensors can also measure the scattering effects of large ice particles that later melt to form raindrops. Based on the radiance contrast between the surface and raindrops at the available passive microwave channels, the GPROF algorithm physically retrieves the vertical hydrometeor profiles that best fit the observed microwave radiance. A library of hydrometer profiles generated by a cloud resolving model is scanned to find which profiles are radiatively compatible with the observations; the retrieved profiles, including the surface rain rates, is a Bayesian composite of the compatible profiles.

All the instantaneous rainfall pixel data are horizontally averaged onto $1^\circ \times 1^\circ$ grid boxes for each individual satellite dataset, and time averaged over 6 h centered on analysis times (0000, 0600, 1200, 1800 UTC). Due to the nearly uniform emissivity of the ocean surface and the large emission contrast between the ocean surface and raindrops, passive microwave remote sensing generally tends to provide more accurate instantaneous rainfall retrievals at the pixel level over the ocean than over the land. However, the grid-box averaged rainfall retrievals from each satellite are only snapshots of a $1^\circ \times 1^\circ$ grid box for duration of a few seconds within the 6h analysis window, instead of “true” 6-h averages. Errors due to under sampling could be equally severe over both the ocean and the land. Nevertheless, the same observational error covariance is applied to the rainfall data over the ocean and the land in both the Tropics and midlatitudes, and to rain estimates from different satellites. Rainfall assimilation is conducted between 50°S and

50°N, so that the impact of satellite rainfall assimilation over different climate regimes, such as land vs. ocean, and midlatitudes vs. Tropics, can be evaluated.

3. The GEOSDAS and 1-D VCA

3a. GEOS DAS3 system

The NASA GEOS3 Data Assimilation System (DAS) is used in this study. It consists of three major components: an atmospheric general circulation model, the Physical-space Statistical Analysis System (PSAS; Cohn et al. 1998), and the Incremental Analysis Update scheme (IAU; Bloom et al. 1996). For each analysis times (0000, 0600, 1200, 1800 UTC), the atmospheric GCM starts 3 hours earlier and runs forward to produces the first-guess fields at the analysis time. The analysis fields and the analysis increments can be computed in a conventional way by ingesting observations within each 6-h window through PSAS. By restarting the short-term forecast, the IAU scheme gradually inserts an equal fraction of the analysis increments at each model time step. Thus the reanalysis is produced with additional tendency corrections that are updated by observations. It is found that significant improvements in terms of assimilation accuracy, noise control, and the hydrologic cycle spin-up are obtained using the IAU technique (Bloom et al. 1996).

The GEOS3 physics uses an interactive land surface model. The moist parameterization includes the relaxed Arakawa-Schubert convective parameterization (Arakawa and Schubert 1974, Moorthi and Suarez 1992) coupled with a re-evaporation of falling anvil rain, as well as large-scale condensational precipitation. The model prognostics and diagnostics are computed at 1x1 deg resolution in horizontal, and there are 48 layers in the vertical extending from the surface to the stratosphere.

3b. 1-D VCA

The 1-D VCA algorithm developed by Hou et al. (2000a, b, 2001, 2004) uses microwave rainfall retrievals to formulate additional IAU forcing on time tendencies of temperature and moisture to compensate for the systematic errors caused by the model moist physics within a 6-h assimilation cycle. The detailed procedure can be found in Hou et al. (2000a, 2004). Essentially,

the 1-D VCA seeks to minimize a functional that measures the misfit between the model-predicted rain and the observed rain with respect to the temperature and moisture time tendencies. For each grid box, the model-predicted rain rate is obtained by performing a 6-h integration of a 1-D column model with moist physics. The time tendencies due to processes other than moist physics, such as advection, turbulence, and radiation, are prescribed from a 3-h forecast by the full GOES DAS3 run from the beginning of the analysis cycle. The minimization is performed at each grid box where the difference between the observed 6-h rain rate and the model-generated rain are larger than 1 mm/day. A prescribed vertical structure of the moisture analysis increment is introduced to mimic the Jacobian of the 6-h mean precipitation with respect to moisture perturbations. Following Hou et al. (2004), the vertical profiles of temperature and moisture time-tendency adjustments are assumed to have the same error standard deviations as q and T in the GEOS DAS3.

Shown in Figure 1 are an example of satellite rainfall retrievals from SSM/I, TMI, and AMSR-E within one 6-h analysis window centered at 06 UTC, July 1, 2002, along with the difference between the column model first guess and the observation, as well as the difference between the column model optimized rainfall and the observation. Although there are still observational gaps within the 6-h analysis window, the 5-satellite constellation has good swath coverage between 50°N and 50°S, and many tropical and midlatitude convective systems can be clearly identified over both the ocean and the land. The rainfall minimization scheme for the column model is effective in bringing the model estimated rainfall toward to the observation, and the reduction in the error std dev is about 32%.

3c. Experimental designs

Three parallel assimilation experiments are performed in this study from July 1 to July 31 2002, with two assimilating rainfall retrievals from the 5-satellite constellation between 50°S and 50°N. During this period, cloud and radiation data from the Moderate Resolution Imaging Spectroradiometer (MODIS, King et al. 2003) and the Clouds and the Earth's Radiant Energy System (CERES, Wielicki et al. 1996, 1998) onboard both EOS TERRA and AQUA are available, and provide a unique opportunity to evaluate the assimilation results with independent, con-current satellite observations on cloud properties and radiative fluxes. The control is the

standard GEOS3 assimilation with conventional observations plus SSM/I TPW observations. Ocean_Only and Ocean+Land are experiments assimilating satellite rainfall observations, with one only assimilating observations over the ocean, and the other assimilating observations over both the ocean and the land. The purpose of these two rainfall assimilation experiments is to examine the benefit of including rainfall retrieval data over the land where rainfall estimations are typically believed to have larger retrieval errors than those over the ocean.

4. Impact on monthly means

4a. Surface precipitation

Satellite retrieved monthly-mean precipitation for July 2002 (Fig. 2a) clearly shows a strong Intertropical Convergence Zone (ITCZ) around 10°N extending from the Pacific Ocean, across the South America and the Atlantic Ocean, into the equatorial African continent. There is another ITCZ over the Indian Ocean and western Pacific about 5-10 degree south of the equator. Heavy precipitation can also be noticed over regions where monsoonal rainfall dominates, such as the southeast of North America, South and East Asia. Moderate precipitation mainly related to baroclinic instabilities can also be seen in higher latitudes in both the hemispheres.

Figures 2b, 2c, and 2d show the monthly-mean co-located differences between satellite observations and online assimilation runs. The control run generally overestimates precipitation over broad areas of the tropical western Pacific, the Caribbean Sea, the northern part of the Amazon Basin, the India Ocean, and the regions surrounding the Tibetan Plateau, and underestimates precipitation over the tropical African continent, the tropical eastern Pacific, and the middle-west part of North America along the Rocky Mountain. The rainfall differences are especially severe over the Caribbean Sea where satellite observations show very little precipitation except over some large islands. Most of the above regions are over open oceans, remote land areas, or near big mountains, where surface observations are few or very sparse and model physical parameterizations may usually fail to capture what occurs in nature. Therefore the big discrepancies over these regions mainly stem from a combination of large systematic errors in the model moist physics, and the lack of conventional observations in the control analysis.

When Ocean_Only and Ocean+Land rainfall observations are assimilated, both experiments show significant improvements around most areas where the data are assimilated, indicating the efficiency of the 1-D VCA algorithm bringing the model analysis toward the observations. Overall, the rainfall assimilation between 50°S and 50°N enhance the spatial correlation of the monthly-mean precipitation with observations from 0.69 to 0.84, and reduce the error STD dev by 30% for the Ocean+Land experiment. These statistics are comparable to those from earlier studies over the Tropics by Hou et al. (2000a, b). Although land observations are not assimilated and rainfall discrepancies over the land are essentially unchanged in Fig. 2c, the Ocean_Only experiment still enhance the spatial correlation of the monthly-mean precipitation to 0.74, and reduce the error std dev by 14%. Similar to what noticed in Hou et al. (2000a, b), the 1-D VCA algorithm tends to be more effective in reducing the precipitation intensity than enhancing it in matching the GEOS analysis with the microwave rainfall retrievals.

Table 2 compares the statistics of the three experiments over the Tropics and the midlatitudes. Here the Tropics is defined as the area between 30°S and 30°N, while the midlatitude is defined as the area between 30° and 50° in the two hemispheres. Table 2 shows that the control experiment tends to overestimate the observed monthly mean rain rate by about 37% in the Tropics, suggesting large model systematic errors in the Tropics where precipitation is mainly governed by the model's convective parameterization. On the other hand, the control experiment tends to underestimate the observation by 8% in midlatitudes where the large-scale precipitating process dominates. As more and more satellite rainfall retrievals covering the extended area are assimilated in the analysis, the error std dev. become smaller, and the correlation between the analysis and the observation increases in both the Tropics and midlatitudes.

Many earlier rainfall assimilation studies only used rainfall retrievals over the ocean since the microwave rainfall estimation over the land usually has larger retrieval errors due to the irregularity of the land surface, and the weak radiance contrast between the land surface and raindrops. A few interesting questions that remain to be explored are: will assimilation of accurate oceanic rainfall observations be beneficial to model analyses over the land at monthly-mean time scales? In other words, even the satellite rainfall retrievals over the land are believed

to have larger retrieval errors (typically in terms of precipitation intensity), do they still have some positive impacts on the model analyses over the land, especially in terms of the location of deep convection? Table 3 compares the precipitation statistics of the three experiments over the ocean and the land, and suggests that at the monthly time scale, the benefit of rainfall assimilation in terms of the precipitation distribution is more or less limited over the area where the observations are actually assimilated in the analysis. For example, the error STD dev and correlation are nearly identical over the ocean for the Ocean_only and Ocean+Land experiments. The precipitation statistics over the land are improved by about 33% only after the rainfall observations over the land are assimilated in the analyses. Therefore, even the current microwave rainfall estimations may have larger retrieval errors over the land than those over the ocean; it is important and helpful to assimilate them to improve model analyses over the land.

4b. Moisture and temperature structure

As discussed in Hou et al. (2000a, b, 2004), the 1-D VCA algorithm compensates for systematic errors in the model moist physics through temperature and moisture tendency corrections. It is found that the moisture tendency correction is much more effective than the temperature tendency correction by bringing the model-predicted rainfall closer to observations. For single points where the model-predicted rain rate overestimates (/underestimates) the observed, the algorithm tends to redistribute the moisture in the vertical so that the low level becomes drier (/more moist) and the upper level becomes more moist (drier).

It is highly desirable that the zonal-mean temperature and moisture structure in the analyses can be evaluated against rawinsonde observations to verify the generalization of the assumed vertical structure of analysis increment. Due to the lack of data, we first examine the zonal mean monthly difference of mixing ratio and temperature structure between the assimilation run and the control in Figure 3. The zonal mean precipitation (Fig. 3a) indicates that while the rain rate in the control run overestimates the observed rain rate by about 2 mm/day in the Tropics between 10°S and 35°N and underestimates the observed rain rate by less than 1 mm/day in midlatitudes of the Northern Hemisphere, the rain rate in the rainfall-assimilation run tends to be in good agreement with the observed, especially in the Tropics. Reduction of the tropical precipitation in the rainfall-assimilation run leads to a drier planetary boundary layer

(PBL) below 900 hPa, and a more moist low troposphere between 700 and 900 hPa, as well as a slightly drier middle and upper troposphere; Increase of the midlatitude precipitation in the Northern Hemisphere leads to a more moist low troposphere below 700 hPa centered near 900 hPa, and a drier atmosphere above centered at 600 hPa. The temperature increment is generally very small in the Tropics and midlatitudes of the Northern Hemisphere, with a weak warming below 800 hPa and a cooling above.

The precipitation observation does not contain explicit information in the vertical. The structure of the analysis increment is mostly determined by the background error covariance and moist physics Jacobian during the minimization. Since the tendency corrections are applied to the non-linear model trajectory, they will have complex impact on the short-term forecasts, and have influence on the subsequent analysis using the forecasts as first guess fields. It is important to monitor the observation minus first-guess residuals in model state variables, particular to their vertical distribution when precipitation assimilation is applied. The monthly mean biases and error standard deviations of the 6-h O – F residuals for temperature and mixing ratio are also computed for the 3 assimilation experiments over the Tropics and extra-tropics, the land and ocean. Since the difference in the temperature biases and error standard deviations are very small, we only show mixing ratio biases and error standard deviations for the control (solid line) and Ocean+Land (dashed line) experiments in Figure 4. The rainfall assimilation, except at 850 hPa for the profiles averaged over midlatitude and land, generally leads to smaller standard deviations of the moisture O – F residual.

4c. Radiative fluxes

The CERES instruments are improved models of the Earth Radiation Budget Experiment (ERBE; Barkstrom 1984) scanner instruments, which can also provide additional cloud and surface flux information (Wielicki et al. 1996, 1998). The CERES ES-8 instantaneous pixel data from EOS TERRA and AQUA are merged and mapped onto a $1^{\circ}\times 1^{\circ}$ grid at 6-h intervals for July 2002 to compare with the Top-of-the-Atmosphere (TOA) radiative fluxes from the GEOS reanalysis.

The cloud radiative forcing, which was defined by Ramanathan et al. (1989) as the difference between the cloudy-sky and the clear-sky fluxes, has been frequently used to evaluate the cloud effect on the climate. However, the observed instantaneous clear-sky flux does not exist under the cloudy-sky situation. Monthly-mean clear-sky fluxes are usually estimated by either using limited observational samples of clear-sky situations within that month, or running a radiation code for no-cloud situations using observed temperature and moisture profiles. In order to better understand the impact of rainfall assimilation on radiative fluxes and clouds, we first evaluate changes in clear-sky radiative fluxes by comparing the rainfall assimilation run with the control run (not shown), and notice that the monthly-mean differences of TOA clear-sky longwave and shortwave fluxes from the two GEOS analyses sampled at CERES swathes are generally very small. Except for some small and scattered land areas, the differences of TOA clear-sky longwave fluxes are generally less than 2 Wm^{-2} , and the differences of TOA clear-sky shortwave fluxes are generally less than 0.5 Wm^{-2} . Such small differences indicate that the clear-sky radiative fluxes are not sensitive to the direct changes in temperature and moisture profiles corrected by rainfall assimilations, at least at monthly time scales.

Figure 5 compares the July TOA cloudy-sky longwave flux from the GEOS Control and Ocean+Land against the observations derived from CERES ES-8. A positive OLR bias exists in both analyses, mainly concentrating in the subtropical and midlatitude landmass, the extratropical ocean in the southern Hemisphere, and the eastern Pacific, as well as the highly convective central Indian Ocean and western Pacific.

The global mean OLR values from the Control and Ocean+Land overestimate the CERES data by 4.4 and 6.3 W m^{-2} , respectively. As expected, the analysis improvement due to rainfall assimilation is generally small over those less convective regions. On the other hand, corresponding to the excessive model precipitation over the Caribbean Sea, the South America Amazon Basin, and the equatorial central Pacific, the OLR from the control run (Fig. 5b) tends to significantly underestimate the observations. The largest discrepancy is more than 40 Wm^{-2} , suggesting an overestimation of cloud population and/or cloud top heights over these regions. After rainfall observations are assimilated (Fig. 5c), the negative OLR bias related to the

excessive precipitation is significantly reduced, and the OLR error STD dev is reduced from 11.9 to 9.3 W m⁻², which is about a 22% improvement.

Analyzed TOA shortwave flux (Fig. 6) generally has large negative bias over the ocean east of the major continent where precipitation is small. This bias is mainly related the systematic errors from the model parameterization of non-precipitating stratocumulus and processes that are not closely related to the precipitating physics, and therefore is difficult to be corrected by the rainfall assimilation scheme. Over the region where the rainfall assimilation has large changes in the analyzed rain rate, the bias in TOA shortwave flux is reduced, and the mean spatial error STD dev is reduced from 37.5 to 31.5 W m⁻².

Therefore, although the clear-sky radiative fluxes are not sensitive to the direct changes in temperature and moisture profiles corrected by rainfall assimilation, improvements in the cloudy-sky longwave and shortwave fluxes in the rainfall-assimilation run clearly imply that these improvements are accomplished mainly through improved model clouds that are very sensitive to small changes in temperature and moisture profiles.

The monthly-mean spatial statistics of GEOS TOA longwave and shortwave fluxes against CERES ES-8 data, in the Tropics and midlatitudes, and over the ocean and the land, are further summarized in Table 4. Similar to what shown in the precipitation statistics, the rainfall assimilation consistently improves the analysis of the TOA radiative fluxes through reducing the error standard deviation and increasing the spatial anomaly correlation. As long as microwave rainfall retrievals are being effectively utilized, the rainfall assimilation tends to have a positive impact on the GEOS analyses on radiation fields.

4d. Clouds

In GEOS3, convective and large-scale cloud fractions, which are used for cloud-radiation computations, are determined diagnostically (L. L. Takacs, personal communication): Convective cloud fractions produced by RAS are proportional to the detrained liquid water amount, while large-scale cloudiness is defined, following Slingo and Ritter (1985), as a function of relative humidity. The total cloud fraction in a grid box is determined by the larger of the two cloud fractions. The MODIS level-2 global cloud products combine advanced infrared and visible

technique to determine both physical and radiative cloud properties (King et al. 2003). The MODIS cloud fraction data are produced by the infrared retrieval methods both day and night at 5x5 1-km-pixel resolution. High-resolution MODIS pixel data from both Terra and Aqua are merged and mapped onto a 1°x1° grid at 6-h intervals for July 2002.

Figure 7 shows the observed MODIS total cloud fraction in unit of percentage, and the differences between GEOSDAS runs and observations. The observed total cloud fraction is generally above 80% in midlatitude storm tracks, and tropical oceans and lands where deep convection dominates. Large total cloud fraction can also be seen in the subtropical oceans west of major continents where non-precipitating stratocumuli persist. These features are quantitatively consistent with earlier climatological data over the ocean from the International Satellite Cloud Climatology Project (ISCCP; Rossow and Schiffer 1991) and the Comprehensive Ocean-Atmosphere Data Set Project (COADS). Over the subtropical African continent, Australia, Middle East and the west coast of North America where the large-scale subsidence dominates and rain rates are generally low, the total cloud fraction is generally below 20%. Over other parts of major continents, the total cloud fraction has large variability, and typically ranges from 30% to 70%. Unlike precipitation and radiative fluxes which show consistent improvements over broad areas after rainfall assimilations, the error std dev. of the total cloud fraction in the rainfall-assimilation run only decreases slightly, partly due to the inclusion of a lot of non-precipitating clouds that are difficult to be modified by the rainfall assimilation. However, over areas where the assimilation run shows significant improvements in precipitation (e.g., the Caribbean Sea), there is indeed evidence that the model total cloud fraction as well as the high cloud fraction (not shown here) become closer to the MODIS observations.

5. Impact on 6-hourly time series

While the monthly-mean comparisons provide valuable information on the physical impact of the rainfall assimilation algorithm, it is possible, however, for the analysis to produce realistic mean states for the wrong reasons. For example, the mean rain rate and its spatial standard deviation can not tell the sequential distributions of intensity and frequency of rain events within an individual month, and it is likely that a region characterized by frequent light

rain events has the same monthly mean rain rate as a region with less frequent but heavier rain events. With enhanced satellite sampling rates, we further evaluate the performance of the 1-D VCA algorithm in this section on 6-hourly time scales over selected climate regimes where (1) the control monthly mean rain rate overestimates the observed, and (2) the control monthly mean rain rate underestimates the observed.

As shown in earlier sections, the rainfall-assimilation run indicates considerable improvements in term of monthly-mean rain rate over the Caribbean Sea where the satellite retrievals show little precipitation. The time series of precipitation at 81°W, 19°N (Figure 8) confirms that the observed rain rate (thin line with open circle) was very small. Except for 3-4 short-duration rain events with rain rates slightly less than 5 mm/day, rain rates at all the other periods were close to zero. The control run significantly overestimates the observed rain rate throughout most of the month, with frequent heavy rain events that may sometimes reach 70 mm/day. The 1-D VCA scheme is in general very effective in bringing the analyzed rain rate toward to the observed, and the root-mean-square (RMS) error reduces from 23.8 to 9.3 mm/day. Corresponding to the reduced rain rate in the assimilation run, the TOA longwave flux increases with a few occasions in which the OLR values may change dramatically from 150 Wm^{-2} to 270 Wm^{-2} . The TOA reflected shortwave flux and high cloud fractions also show reasonable reductions, and are in better agreements with radiation and cloud data derived from CERES and MODIS.

Similar plots over the tropical African continent (21°E, 8°N) where the control tends to underestimate the observed rain rate (Figure 9) indicate that several deep convective rain events occurred in early and late July are totally missed in the control analysis, possibly due to the lack of conventional surface and upper-air observations. The model moist physics only produces a few scattered light to moderate rain events over this tropical rain forest area where deep convection frequently occurs. The TOA radiative fluxes and high cloud fraction also suggest similar bias. After satellite rainfall retrievals are assimilated, the big rain events can be clearly

noticed, and the sequence of convective development over the tropical summer continent is in better agreement with the observations.

Another interesting climate regime is over the western Pacific warm pool where the control run overestimates the observed monthly-mean rainfall by about 4-8 mm/day. Figure 10 shows the 6-hourly time series of precipitation, along with the difference of mixing ratio, TOA longwave and shortwave fluxes between the rainfall assimilation run and the control run at 160°E, 10°N. Satellite rainfall retrievals show that there were a series major precipitating systems passing by the grid box between July 3rd and July 7th, 2002. Except for two 2-day disturbances around July 15th and July 18th, the warm pool was generally dominated by light-rain events following the passage of the early-July major convective system. These features appear to be similar to the earlier findings from the Tropical Ocean Global Atmosphere Couple Ocean-Atmosphere Experiment (TOGA COARE, Webster and Lukas 1992) that following major convective events associated with the westerly wind burst, there was usually a long period of clear-sky light wind situations with scattered shallow cumuli and trade wind clouds dominating over the warm pool (Lin and Johnson 1996, Johnson and Lin 1997). Re-evaporation of these episodic shallow clouds tends to gradually moisten the lower troposphere, along with slowly recovering sea surface temperatures, providing a favorable condition for organized deep convection to occur at later times. Such a sequence has also been considered as a possible mechanism (Blade and Hartmann 1992, Kemball-Cook and Weare 2001) to explain the onset and development of the Intra-seasonal Oscillation (ISO, Madden and Julian 1972, 1994). In contrast, the control run shows frequent, heavy rain events over the warm pool with rain rates typically above 20 mm/day during the observed light-rain periods, a clear indication that the convection parameterization used in GEOSDAS tends to produce too many deep convective clouds that generate frequent heavy-precipitating events. After the rainfall assimilation, the analyzed rain rates generally agree better with the observed, especially during the light rain period in mid- and late July. The vertical mixing ratio difference plot clearly indicates more drying in the PBL which

suppresses the population of deep convective clouds, and more moistening at lower troposphere which could be caused by enhanced evaporation from an increased shallow cumuli population. In addition, both TOA longwave and shortwave fluxes show reduced RMS errors. Although it is outside of the focus of this study, we can expect that the intraseasonal signals, which are not well presented in many GCMs and operational model reanalyses, will be better illustrated in the rainfall assimilation analysis.

In summary, physical parameterizations of moist processes used in climate and NWP models are formulated under simplified assumptions and conditions using observations from limited field experiments, and may have large systematic errors in different climate regimes. At regions where the model moist physics tend to behave badly under distinctly different raining regimes, not only is the analyzed rain rate brought closer to the observed, but also the thermodynamic and cloud radiative features are more physically consistent. These provide some solid evidence that the 1-D VCA algorithm can indeed compensate for some of the systematic errors in the model's moist physics.

6. Impact on the analysis and forecast of a midlatitude frontal system

Improving analysis and forecasting skills on various weather events is the ultimate goal of data assimilation and it also serves as an important test for the assimilation algorithm and model physics. Since Hou et al. (2004) has examined the impact of the 1-D VCA algorithm on hurricane forecasts and found that the rainfall assimilation led to more realistic hurricane structure and better 5-day hurricane track prediction and precipitation forecasts, in this section we perform a similar analysis to further explore the impact of rainfall assimilation on improving the synoptic analysis and forecast of a midlatitude frontal system.

6a. Frontal system history and the impact on synoptic analysis

In Figure 11, satellite rainfall retrievals, and the analyzed precipitation, 200 hPa wind vectors, and 500 hPa geopotential heights, as well as their differences between the control and rainfall-assimilation runs are presented to illustrate the evolution of the midlatitude frontal system from 18 UTC, 4 July to 18 UTC, 9 July 2002. In the northern hemisphere summer, a strong subtropical high persists over the eastern Pacific. It usually interacts with the eastward-propagating midlatitude baroclinic waves by transporting the lower-latitude moisture northward and forms frontal-like convective systems. At 18 UTC, 4 July (Fig. 11a), observations show a large, northeast-southwest oriented rain band near the Dateline extending from 170°E to 170°W. There was another bow-shaped precipitating system at 140°W which was related to a dissipating frontal system developed at an earlier time but will not be discussed in this study.

Both the control and precipitation analyses show the rain band near the Dateline at about the right observed position, although rainfall was more scattered and less intensive in the control analysis. The largest discrepancies are in the fields of 500 hPa geopotential height and 200 hPa wind: the control run shows a strong subtropical high with a ridge extending deeply into midlatitudes. The rain band was located close to the west side of the subtropical high center with strong-wind areas behind. After a few days of continuous rainfall assimilations starting at 00Z, 1 July, the precipitation analysis at 18Z, 4 July shows a more reasonable thermodynamic and kinematic structure: 500 hPa geopotential height shows a low in midlatitudes centering at 175°E, 46°N, with the subtropical high centered at 160°W, 30°N. The frontal rain band was located in between the low and high, and was characterized by large temperature gradients and strong southwesterly enhanced by both the cyclonic flow by the low and the anticyclonic flow by the high.

As the midlatitude low gradually moved eastward with time, the cyclonic flow was decoupled with the anticyclonic flow surrounding the subtropical high. The rain band was separated into two parts with the southwest part staying on the west side of the stationary subtropical high and the northeast part behaving as a midlatitude frontal system continuously moving eastward

along with the midlatitude wave. At 1800 UTC, 7 July (Fig. 11b), the midlatitude frontal rain band evolved in a spiral form around a low in 500 hPa geopotential height. Both the control and rain-assimilation analyses show a deepening low centered at 155°W , 47°N with similar order of amplitudes. While the frontal rainfall distribution in the precipitation analysis is in good agreement with the observed, the control only shows two small raining areas in front of the trough. This underestimation problem persists in the control analysis when the frontal system reached its mature stage at 06 UTC, 8 July (Fig. 11c), although the large-scale features such as the 500 hPa geopotential height and the 200 hPa wind vector appear to be similar between the control and rainfall-assimilation runs. Again, the frontal rain band in the rainfall-assimilation run is better presented, and agrees well with the satellite observations in terms of the system position and precipitating intensity. As the system continuously propagated eastward along with midlatitude westerlies (Fig.11d), the low started to weaken as it approached the west coast of North America, with another heavy raining system entering the selected domain from the west.

Figure 12 further shows the rms errors and spatial correlations of 6-hourly averaged rain rate from the control (solid lines) and rainfall-assimilation (dashed lines) analyses, respectively, with combined satellite rainfall retrievals used for verifications. After rainfall assimilations, the rainfall rms errors associated with the midlatitude frontal system are reduced by about 1-3 mm/day, and the correlation increased from 0.35 to 0.6, a 50% improvement.

As shown in Figure 11c, the observed frontal rain band was oriented in the northeast-southwest direction with relatively uniform precipitation rates (15 mm/day) along the front at 0600 UTC 8 July. At this stage, the control analysis shows little precipitation at the leading edge of the front, while the rainfall-assimilation run agrees well with observations. Since the control and the rainfall assimilation runs show drastic differences in precipitation, we focus on this time to examine the impact of rainfall-assimilation on the vertical structure of the frontal system.

Figure 13 shows vertical cross sections of temperature, mixing ratio, relative vorticity, and vertical motion from the control and the rainfall-assimilation runs across the frontal system

between 153°W, 47°N and 140°W, 36°N, along with their differences. Analyzed surface precipitation is also included to indicate the location of the frontal rain band for both control and rainfall-assimilation runs. Associated with enhanced frontal precipitation in the rainfall-assimilation run, temperature is increased by 0.5-2 K at low levels between 975 and 900 hPa, and decreased by 0-1 K above between 850 and 400 hPa in the raining areas. Correspondingly, mixing ratio is also increased by about 1-2 g/kg at low levels and decreased by 0-1 g/kg between 800 and 650 hPa over the raining area. Such a large increase in both temperature and moisture at low levels, along with a cooler middle troposphere, significantly increase the convective available potential energy (CAPE) and lead to a stronger upward motion in the rainfall-assimilation run. The omega plot clearly indicated an enhanced upward motion resulted from the rainfall assimilation with amplitude of 100 hPa/day at the leading edge of the front. Larger positive vorticity can also be noticed, especially at low levels.

Behind the frontal rain band, although neither observations nor analyses show any precipitation, the impact of rainfall assimilation on the thermodynamic and kinematic structure of the midlatitude frontal system is still very prominent. The rainfall-assimilation run indicates a temperature decrease of about 0-1 K at both the low level and between 650 and 400 hPa. Compared with the control run, there is a larger temperature gradient, which suggests an enhanced frontogenesis, at low levels across the front with an amplitude of 1K/100 km at about 925 hPa. The moisture difference plot shows an interesting feature: mixing ratio is increased by 1-2 g/kg at low levels behind the frontal rain band but capped by a strong drying between 650 and 800 hPa, and such a low-level moisture increase can extend several hundred kilometers behind. One possible explanation is that the rain evaporation tends to increase the low-level moisture but it is capped by strong large-scale downward motion behind the frontal rain band, as seen in Figure 13b.

6b. Impact on the forecast

Since the rainfall assimilation can modify the analyzed thermodynamic and kinematic fields, especially at low levels, so that they are more physically and dynamically consistent with observations, we perform parallel forecasts on this midlatitude frontal system initialized with the control and rainfall analyses to further examine the impact of these changes on the forecasts. As shown in Figure 12 that the rainfall-assimilation analysis generally have lower RMS errors and higher spatial correlations in precipitation than the control run within a 25° in latitude x 60° longitude domain, we issue four 5-day forecasts 24 h apart using the initial conditions from 0300 UTC 5 July to 0000 UTC 8 July 2002, and the rainfall-assimilation analyses are used for verifications.

Figure 14 show the RMS and anomaly correlation of a 5-day forecast of sea level pressure, precipitation, and 500 hPa geopotential height initialized using 0300 UTC 6 July analyses. The RMS errors and anomaly correlation of forecasted sea level pressure associated with the midlatitude frontal system are very similar between the control and rainfall-assimilation runs. Similar plots for the 500 hPa geopotential height also indicate similar RMS errors and anomaly correlations for the first 3-day forecasts, but the rainfall assimilation run tends to have a significantly smaller RMS errors and higher correlations at Day 4 and Day 5. The precipitation forecast initialized from the rainfall-assimilation analysis indicates some improved forecasting skills over the control during the first 1-2 days, but the forecasting skill for the midlatitude frontal system shows little improvement.

7. Summary and Conclusions

In earlier studies, a 1-D VCA algorithm was developed to assimilate 6-h averaged rainfall observations over tropical oceans in the GEOS3 DAS (Hou et al. 2001a, b, 2004), with a focus to improve tropical analyses and forecasts. This 1-D VCA scheme uses temperature and moisture tendency corrections as control variables to minimize the misfit between the observed- and the model-predicted rain rates. Through a gradual insertion of additional temperature and moisture forcing resulted from the rainfall assimilation, the scheme can effectively compensate

for some model deficiencies due to imperfect moist physics so that the tropical analysis and forecast are more physically and dynamically consistent with observations.

With enhanced satellite rainfall observations available, this study explores the performance of the rainfall assimilation algorithm over broad areas of the globe, and extends the investigation over tropical oceans into the extratropics where the atmospheric processes are governed by the quasi-geostrophic dynamics and large-scale condensational precipitation processes, and land areas where microwave rainfall estimations are believed to be less accurate than those over oceans.

Satellite microwave rainfall retrievals from a 5-satellite constellation, including TRMM TMI, SSM/I from DMSP F13, F14 and F15, and AMSR-E on EOS-AQUA, are assimilated into the NASA GEOSDAS. Three parallel assimilation runs, namely, the Control for the run with only conventional observations assimilated, the Ocean_Only and Ocean+Land standing for the assimilation run with/without rainfall assimilation over the land, are conducted and compared with each other. The physical and dynamical impact of rainfall assimilations on the GEOS reanalyses are evaluated against independent satellite observations over both the Tropics and midlatitudes at different temporal and spatial scales.

Monthly-mean results indicate that large rainfall discrepancies between the Control and observations mainly stem from a combination of large systematic errors in the model moist physics, and the lack of conventional observations in the control analysis. When microwave rainfall retrievals are assimilated, there are significant improvements in the precipitation analysis over most areas where the rainfall data are assimilated. The 1-D VCA algorithm, through compensating for systematic errors in the model moist physics, is effective over both the Tropics and extratropics where the atmospheric processes are dominated by different dynamics and moist physics, and the ocean and the land where rainfall observations have different retrieval error characteristics. Although the rainfall estimation over midlatitudes and land areas may have larger retrieval errors than those over tropical oceans, assimilating the microwave rainfall information still has large positive impacts on the GEOS analysis. This will provide important guidance for a more effective use of satellite rainfall measurements over the entire globe.

Model diagnosed TOA longwave and shortwave fluxes, and total cloud fractions are evaluated against independent satellite observations from CERES and MODIS. Although the

model cloud parameterization has large systematic errors that are difficult to be corrected by the rainfall assimilation alone, TOA longwave and shortwave fluxes, and cloud fractions do indicate noticeable improvements, in particular over regions where rainfall analysis shows significant improvements.

The physical and dynamical impact of rainfall assimilation on the GEOS analysis are further evaluated on 6-h time scales over selected regions where the model moist physics tends to behave badly under distinctly different raining regimes. In particular, over the western Pacific warm pool where the model moist physics tends to produce frequent, excessive precipitation with unrealistically large amount of deep convective clouds, the rainfall assimilation tends to constrain the vigorous development of deep convective clouds by drying the PBL while at the same time force more shallow cumuli over a prolonged period to moisten the lower troposphere, thus providing a favorable condition for organized deep convection to occur later. These features are consistent with earlier observational studies on the tropical hydrologic cycle associated with the intraseasonal oscillation and westerly wind burst. It is well known that many GCMs tend to precipitate too much, and too frequently over the warm pool, and have difficulties to well represent important tropical waves such as the intraseasonal oscillation. The precipitation assimilation, which uses rainfall information to correct some biases in the model moist physics, may provide a good opportunity to better understand and correct the model physical deficiencies.

The impact of assimilation experiments with and without rainfall data on the analysis and forecast of a midlatitude frontal system clearly indicate that the improved rainfall analysis is achieved through reasonable changes in the thermodynamic and dynamic fields that respond to the rainfall assimilation. The synoptic structure of temperature, moisture, winds, divergence, and vertical motion, as well as vorticity is more realistically oriented across the front, and the influence of rainfall assimilation can extend a few hundred kilometers outside of the raining area. Short-term forecasts using initial conditions assimilated with rainfall data also give slightly improved results.

Further work is underway to investigate the physical and dynamical impact of rainfall assimilation at the intraseasonal and diurnal time scales.

Acknowledgments

The TRMM TMI, DMSP SSM/I, MODIS TERRA and AQUA data were provided by the NASA Goddard Space Flight Center Data Archive and Distribution Center. The CERES data were provided by the NASA Langley Center Data Archive and Distribution Center. The AMSR-E data were provided by the National Snow and Ice Data Center Distributed Active Archive Center. Many thanks to Dr. Chris Kummerow (CSU), and Ralph Ferraro (NOAA) for their kind help on the AMSR-E data processing. Thanks to Dr. Bill Olson (GSFC) for providing much valuable insights and critical comments to an early version of the manuscript. This research has been supported by NASA Precipitation Measurement Missions Research under WBS 51-621-15-45 and Interdisciplinary Science Research under WBS 51-291-01-C7.

Figure Legends

Figure 1: (a) The 6-h averaged satellite rainfall retrievals (mm/day) from TRMM TMI, DMSP F13 and F14 SSM/I, EOS AQUA AMSR-E at 0600 UTC on 1 July 2002; (b) Rainfall difference between the satellite rainfall observation and the column model first guess sampled at satellite ground tracks; (c) Rainfall difference between the satellite rainfall observation and the column model optimized rainfall sampled at satellite ground tracks.

Figure 2: (a) Time-mean satellite rainfall retrievals for July 2002; (b) Difference between satellite rainfall estimates and precipitation from the control sampled at satellite observations; (c) Same as (b) but for the Ocean_only experiment; (d) same as (b) but for the Ocean+Land experiment. Also shown are the computed spatial anomaly correlation (AC), bias, and error standard deviation.

Figure 3: (a) Zonal mean rainrates (mm/day) from satellite rainfall retrievals (solid line), the control (dotted line) and the rainfall-assimilation (dashed line) runs for July 2002; (b) Zonal mean difference of mixing ratio (g/kg) between the rainfall-assimilation and the control runs; (c) Zonal mean difference of temperature (K) between the rainfall-assimilation and the control runs.

Figure 4: Mixing ratio O – F residuals (bias and error standard deviation) against rawinsonde data over the Tropics and extra-tropics, ocean and land (50°S to 50°N, July 2002): control (solid line) and Ocean+Land (dashed line).

Figure 5: (a) Observed monthly-mean longwave flux (W m^{-2}) from CERES ES-8 for July 2002; (b) Difference of July-mean longwave flux between the control run and the observed; (c) Difference of July-mean longwave flux between the rainfall-assimilation run and the observed.

Figure 6: Same as Figure 5, but for TOA shortwave flux for July 2002.

Figure 7: (a) Monthly-mean total cloud fraction (%) from MODIS, (b) Control minus observation, and (c) Ocean+Land minus observation.

Figure 8: Time series of precipitation (mm/day), TOA longwave and shortwave fluxes (W m^{-2}), and high cloud fraction (%) for a grid point in the Caribbean Sea (81°W, 19°N) where the control run monthly-mean rain rate overestimates the observed. Observation (thin line with open circle),

the control run (thick dashed line), and the rainfall-assimilation run (thick solid line).

Figure 9: Same as Figure 8, except for a grid point in the tropical African Continent (21°E, 8°N) where the control run monthly-mean rain rate underestimates the observed.

Figure 10: Time series of precipitation (mm/day), difference of vertical mixing ratio profile (g/kg), OLR (W m^{-2}), and OSR (W m^{-2}) between the rainfall-assimilation and the control run for a grid point in the western Pacific (160°E, 10°N) where the control run monthly-mean rain rate overestimates the observed. Observation (thin line with open circle), the control run (thick dashed line), and the rainfall-assimilation run (thick solid line).

Figure 11: (i) Satellite rainfall retrievals (mm/day); (ii) surface rain rate (mm/day), 500 hPa geopotential height (m), 200 hPa wind (m/s) from the control analysis; (iii) same as (b) but for the rainfall-assimilation analysis; (iiii) differences of surface rain rate, 500 hPa geopotential height, and 200 hPa wind between the rainfall-assimilation and the control runs, from 1800UTC, 4 July to 1800 UTC 9 July.

Figure 12: RMS errors and spatial correlation of 6-hourly averaged rain rate from the control (solid lines) and rainfall-assimilation (dashed lines) analyses, respectively. Combined satellite rainfall retrievals are used for verification.

Figure 13: Vertical cross sections of temperature (K), mixing ratio (g/kg), relative vorticity (10^{-6} s^{-1}) and vertical motion (hPa/day) and their differences across the midlatitude frontal system.

Figure 14. RMS errors and spatial correlation of 5-day forecasts of a midlatitude frontal system initialized from the control (solid lines) and rainfall-assimilation (dashed lines) analyses, respectively.

References

- Andersson, E., and Co-authors, 2005: Assimilation and modeling of the atmospheric hydrologic cycle in the ECMWF forecasting system. *BAMS.*, 86, 387-402.
- Arakawa, A, and W. H. Schubert, 1974: Interaction of a cumulus cloud ensemble with the large-scale environment,. Part I. *J. Atmos. Sci.*, 31, 674-701.
- Bloom, S. C., L. L. Takacs, A. M. da Silva, and D. V. Ledvina, 1996: Data assimilation using incremental analysis updates. *Mon. Wea. Rev.*, 124, 1256-1271.
- Barkstrom, R. B., 1984: The Earth Radiation Budget Experiment (ERBE). *BAMS*, 65. 1170-1185.
- Chang, S. W., and T. R. Holt, 1994: Impact pf assimilating SSM/I rainfall rates on numerical prediction of winter cyclone. *Mon. Wea. Rev.*, 122, 151-164.
- Cohn, S. E., A. da Silva, J. Guo, M. Sienkiewicz, and D. Lamich, 1998: Assessing the effects of data selection with the DAO physical-space statistical analysis system. *Mon. Wea. Rev.*, 126, 2913-2926.
- Derber, J. C., 1989: A variational continuous assimilation technique. *Mon. Wea. Rev.*, 117, 2437-2446.
- Errico, R. M., L. Fillion, D. Nychka, and Z.-Q. Lu, 2000: Some statistical considerations associated with the data assimilation of precipitation observatons. *Quart. J. Roy. Meteor. Soc.*, 126A, 339-359.
- Fillion, L., 2002: Variational assimilation of precipitation data and gravity wave excitation. *Mon. Wea. Rev.*, 130, 357-371.
- Fillion, L., and R. Errico, 1997: Variational assimilation of precipitation data using moist convective parameterization schemes: A 1D-Var study. *Mon. Wea. Rev.*, 125, 2917-2942.
- Fillion, L., and J.-F. Mahfouf : Coupling of moist-convective and stratiform precipitation

processes for variational data assimilation, *Mon. Wea. Rev.*, 128, 109-124.

Hou, A. Y., D. V. Ledvina, A. M. Da Silva, S. Q. Zhang, J. Joiner, R. Atlas, G. J. Huffman, and C. D. Kummerow, 2000a: Assimilation of SSM/I-derived surface rainfall and total precipitable water for improving the GEOS analysis for climate studies. *Mon. Wea. Rev.*, 128, 509-537.

Hou, A. Y., S. Q. Zhang, A. M. Da Silva, W. S. Olson, 2000b: Improving assimilated global datasets using TMI rainfall and columnar moisture observations. *J. Climate*, 13, 4180-4195.

Hou, A. Y., S. Q. Zhang, A. M. Da Silva, W. S. Olson, C. D. Kummerow, and J. Simpson, 2001: Improving global analysis and short-range forecast using rainfall and moisture observations derived from TRMM and SSM/I passive microwave sensors. *Bull. Amer. Meteor. Soc.*, 82, 659-679.

Hou, A. Y., S. Q. Zhang, A. M. da Silva, W. S. Olson, C. D. Kummerow, J. Simpson, 2002: Improving global analysis and short-range forecast using rainfall and moisture observations derived from TRMM and SSM/I passive microwave sensors. *American Meteorological Society*, 82, 659-679.

Hou, A. Y., S. Q. Zhang, and O. Reale, 2004: Variational continuous assimilation of TMI and SSM/I rain rates: Impacts on GEOS-3 hurricane analyses and forecasts. *Mon. Wea. Rev.*, 2094-2109.

Blade, I, and D. L. Hartmann, 1993: Tropical intraseasonal oscillations in a simple nonlinear model. *J. Atmos. Sci.*, 50, 2922-2939.

Johnson, R. H., and X. Lin, 1997: Episodic trade wind regimes over the western Pacific warm pool. *J. Atmos. Sci.*, 54, 2020-2034.

Kemball-Cook, S. R., and B. C. Weare, 2001: The onset of convection in the Madden-Julian Oscillation. *J. Climate*, 14, 780-793.

King, M. D., W. P. Menzel, Y. J. Kanfman, D. Tanre, B. C. Gao, S. Platnick, S. A. Ackerman, L. A. Remer, R. Pincus, and P. A. Hubanks, 2003: Cloud and aerosol and water vapor properties,

precipitable water, and profiles of temperature and humidity from MODIS. *IEEE Transactions Geoscience and Remote Sensing*, 41, 442-458.

Krishnamurti, T. N., C. M. Kiishtawal, Z. Zhang, T. LaRow, D. Bachiochi, E. Williford, S. Gadgil and S. Surendran, 2000a: Multimodel ensemble forecasts for weather and seasonal climate. *J. Climate*, 13, 4196-4216.

Krishnamurti, T. N., C. M. Kiishtawal, D. W. Shin and C. E. Williford, 2000b: Improving tropical precipitation forecasts from a multianalysis superensemble. *J. Climate*, 13, 4217-4227.

Kummerow C., W. Barnes, T. Kozu, J. Shiue, and J. Simpson, 1998: The Tropical Rainfall Measuring Mission (TRMM) sensor package. *J. Atmos. Ocean Tech.*, 15, 809-817.

Kummerow C., Y. Hong, W. S. Olson, S. Yang, R. F. Adler, J. McCollum, R. Ferraro, G. Petty, D.-B. Shin, and T. T. Wilheit, 2001: The evolution of the Goddard Profiling Algorithm (GPROF) for rainfall estimation from passive microwave sensors. *J. Appl. Meteor.*, 40, 1801-1820.

Lin, X., and R. H. Johnson, 1996: Heating, moistening, and rainfall over the western Pacific warm pool during TOGA COARE. *J. Atmos. Sci.*, 53, 3367-3383.

Macpherson, B., 2001: Operational experience with assimilation of rainfall data in the Met Office mesoscale model. *Meteor. Atmos. Phys.*, 76, 3-8.

Madden, R. A., and P. R. Julian, 1972: Description of global-scale circulation cells in the Tropics with a 40-50 day period. *J. Atmos. Sci.*, 1109-1123.

Madden, R. A., and P. R. Julian, 1994: Observations of the 40-50-day tropical oscillation-A review. *Mon. Wea. Rev.*, 122, 814-837.

Marecal, V., and J. -F. Mahfouf, 2000: Variational retrieval of temperature and humidity profiles from TRMM precipitation data. *Mon. Wea. Rev.*, 128, 3853-3866.

Marecal, V., and J. -F. Mahfouf, 2002: Four-dimensional variational assimilation of total column water vapour in rainy areas. *Mon. Wea. Rev.*, 130, 43-58.

Marecal, V., J. –F. Mahfouf, and P. Bauer, 2002: Comparison of TMI rainfall estimates and their impact on 4D-Var assimilation. *QJRM*, 128, 2737-2758.

Marecal, V., and J. –F. Mahfouf, 2003: Experiments on 4D-Var assimilation of rainfall data using an incremental formulation. *QJRM*, 129, 3137-3160.

Moorthi, S., and M. J. Suarez, 1992: Relaxed Arakawa-Schubert . A parameterization of moist convection for general circulation models. *Mon. Wea. Rev.*, 120, 978-1002.

Moreau, E., P. Lopez, P. Bauer, A. M. Tompkins, M. Janiskova, and F. Chevallier, 2004: Variational retrieval of temperature and humidity profiles using rates versus microwave brightness temperature. *QJRM*, 130, 827-852.

Nitta, T., and S. Esbensen, 1974: Heat and moisture budget analyses using BOMEX data. *Mon. Wea. Rev.*, 102, 17-28.

Olson, W. S., C. D. Kummerow, G. M. Heymsfield and L. Giglio, 1996: A method for combined passive-active microwave retrievals of cloud and precipitation profiles. *J. Appl. Meteor.*, 35, 1763-1789.

Olson, W. S., C. D. Kummerow, Y. Hong, and W.-K. Tao, 1999: Atmospheric latent heating distributions in the Tropics derived from satellite passive microwave radiometer measurements. *J. Appl. Meteor.*, 38, 633-664.

Olson, W. S., C. D. Kummerow, S. Yang, G. W. Petty, W.-K. Tao, T. L. Bell, S. A. Braun, Y. Wang, S. E. Lang, D. E. Johnson, and C. Chiu, 2005: Precipitation and latent heating distributions from satellite passive microwave radiometry. Part I: Improved method and uncertainties. Submitted to *J. Appl. Meteor.*

Pu, Z., W. –K. Tao, S. Braun, J. Simpson, Y. Jia, J. Halverson, W. Olson and A. Y. Hou, 2002: The impact of TRMM data on mesoscale numerical simulation of super typhoon Paka. *Mon. Wea. Rev.*, 130, 2448-2458.

Pu, Z. and W. –K. Tao, 2004: Mesoscale assimilation of TMI rainfall data with 4DVAR:

sensitivity studies. *J. Meteor. Soc. Japan*, 82, 1389-1397.

Ramanathan, C., R. D. Cess, E. F. Harrison, 1989: Cloud-radiative forcing and climate: Results from the earth radiation budget experiment. *Science*, 243, 57-63.

Rossow W. B., and R. A. Schiffer, 1991: ISCCP cloud data products. *BAMS*, 72, 2-20.

Simpson, J., R. F. Adler, and G. R. North, 1988: Proposed tropical rainfall measuring mission (TRMM) satellite. *Bull. Amer. Meteor. Soc.*, 69, 278-295.

Simpson, J., C. Kummerow, W.-K. Tao, and R. F. Adler, 1996: On the Tropical Rainfall Measuring Mission (TRMM). *Meteorol. Atmos. Phys.*, 60, 19-36.

Slingo, J. M., and B. Ritter, 1985: Cloud prediction in the ECMWF. model. ECMWF Tech. Report No. 46, European Center for. Medium-Range Weather Forecasts, Reading.

Treadon, R. E., 1997: Assimilation of satellite derived precipitation estimates with the NCEP GDAS. Ph.D dissertation, The Florida State University, 348pp.

Tsuyuki, T., 1996a: Variational data assimilation in the Tropics using precipitation data. Part I: Column model. *Meteor. Atmos. Phys.*, 60, 87-104.

Tsuyuki, T., 1996b: Variational data assimilation in the Tropics using precipitation data. Part II: 3D model. *Mon. Wea. Rev.* 124, 2545-2561.

Tsuyuki, T., 1997: Variational data assimilation in the Tropics using precipitation data. Part III: Assimilation of SSM/I precipitation rates, *Mon. Wea. Rev.* 125, 1447-1464.

Webster, P. J., and R. Lukas, 1992: TOGA COARE: The Coupled Ocean-Atmosphere Response Experiment. *Bull. Amer. Meteor. Soc.*, 73, 1377-1416.

Wielicki, B. A., B. R. Barkstrom, E. F. Harrison, and co-authors, 1996: Clouds and the Earth's

Radiant Energy System (CERES): An earth observing system experiment. BAMS, 77, 853-868.

Wielicki, B. A., B. R. Barkstrom, B. A. Baum, and co-authors, 1998: Clouds and the Earth's Radiant Energy System (CERES): Algorithm overview. IEEE Transactions on Geoscience and Remote Sensing, 36, 1127-1141.

Xiao, Q., X. Zou, and Y.-H. Kuo, 2000: Incorporating the SSM/I-derived precipitable water and rainfall rate into a numerical model: A case study for the ERICA IOP-4 cyclone. Mon. Wea. Rev., 128, 87-108.

Zou, X., and Y. H. Kuo, 1996: Rainfall assimilation through an optimal control of initial and boundary condition in a limited-area mesoscale model. Mon. Wea. Rev., 124, 2859-2882.

Zupanski, D., and F. Mesinger, 1995: Four-dimensional variational assimilation of precipitation data. Mon. Wea. Rev., 123, 1112-1127.

Zupanski, M., D. Zupanski, T. Vukicevic, K. Eis and T. Vonder Haar, 2005: CIRA/CSU four-dimensional variational data assimilation system. Mon. Wea. Rev., 133, 829-843.

	Swath width (km)	Equatorial crossing time	Microwave channels	Microwave frequencies
TRMM TMI	760	variable	5	5
DMSP F13 SSM/I	1700	6:16 AM	7	4
DMSP F14 SSM/I	1700	8:20 AM	7	4
DMSP F15 SSM/I	1700	9:27 AM	7	4
EOS AQUA AMSR-E	1700	13:30 PM	12	6

Table 1: Characteristics of satellites and sensors that provide microwave rainfall retrievals.

Tropics	Mean (mm/day)	Bias (mm/day)	Std. Dev (mm/day)	Correlation
Observation	2.788			
Control	3.834	1.0453	3.382	0.7078
Ocean only	3.081	0.2931	2.950	0.7521
Ocean+land	2.895	0.1066	2.250	0.8536

Midlatitude	Mean (mm/day)	Bias (mm/day)	Std. Dev (mm/day)	Correlation
Observation	2.322			
Control	2.147	-0.1750	1.812	0.5957
Ocean only	2.202	-0.1201	1.677	0.6686
Ocean+land	2.123	-0.1985	1.342	0.7670

Table 2. Monthly mean spatial statistics of GEOS precipitation for the three experiments: control, ocean_only, and ocean+land in the Tropics and midlatitude.

Ocean area	Mean (mm/day)	Bias (mm/day)	Std. Dev (mm/day)	Correlation
Observation	2.640			
Control	3.397	0.7566	2.587	0.7520
Ocean only	2.767	0.1271	1.763	0.8853
Ocean+land	2.731	0.0904	1.793	0.8804

Land area	Mean (mm/day)	Bias (mm/day)	Std. Dev (mm/day)	Correlation
Observation	2.599			
Control	2.829	0.2304	3.831	0.5785
Ocean only	2.790	0.1909	4.028	0.5694
Ocean+land	2.344	-0.2544	2.409	0.7588

Table 3. Monthly mean spatial statistics of GEOS precipitation for the three experiments: control, ocean_only, and ocean+land over the ocean and the land.

Tropics	Mean		Bias		Std. Dev.		Correlation	
	OLR	OSR	OLR	OSR	OLR	OSR	OLR	OSR
Observation	262.3	112.7						
Control	265.4	113.8	3.1	1.1	13.2	41.7	0.893	0.621
Ocean_only	267.7	107.9	5.4	-4.8	11.0	35.4	0.923	0.697
Ocean+land	267.9	106.5	5.6	-6.2	10.0	34.9	0.938	0.686

Midlatitude	Mean		Bias		Std. Dev.		Correlation	
	OLR	OSR	OLR	OSR	OLR	OSR	OLR	OSR
Observation	243.1	111.1						
Control	249.8	95.1	6.7	-15.9	8.5	24.6	0.950	0.774
Ocean_only	250.3	94.3	7.1	-16.7	8.2	23.2	0.953	0.795
Ocean+land	250.4	93.3	7.2	-17.7	7.2	22.1	0.965	0.807

Ocean	Mean		Bias		Std. Dev.		Correlation	
	OLR	OSR	OLR	OSR	OLR	OSR	OLR	OSR
Observation	252.2	103.0						
Control	255.4	101.6	3.20	-1.4	10.6	38.6	0.926	0.582
Ocean_only	257.7	96.4	5.47	-6.6	8.1	32.2	0.960	0.657
Ocean+land	257.6	96.5	5.39	-6.6	8.1	32.1	0.960	0.658

Land	Mean		Bias		Std. Dev.		Correlation	
	OLR	OSR	OLR	OSR	OLR	OSR	OLR	OSR
Observation	264.1	137.1						
Control	271.8	122.3	7.8	-14.8	14.2	32.0	0.899	0.763
Ocean_only	271.8	121.3	7.8	-15.8	14.3	31.0	0.900	0.776
Ocean+land	272.4	116.7	8.4	-20.4	11.3	27.0	0.937	0.792

Table 4: Monthly-mean spatial statistics of GEOS TOA long wave and short wave fluxes for the three experiments: control, ocean_only, and ocean+land in the Tropics and midlatitudes, over the ocean and the land.

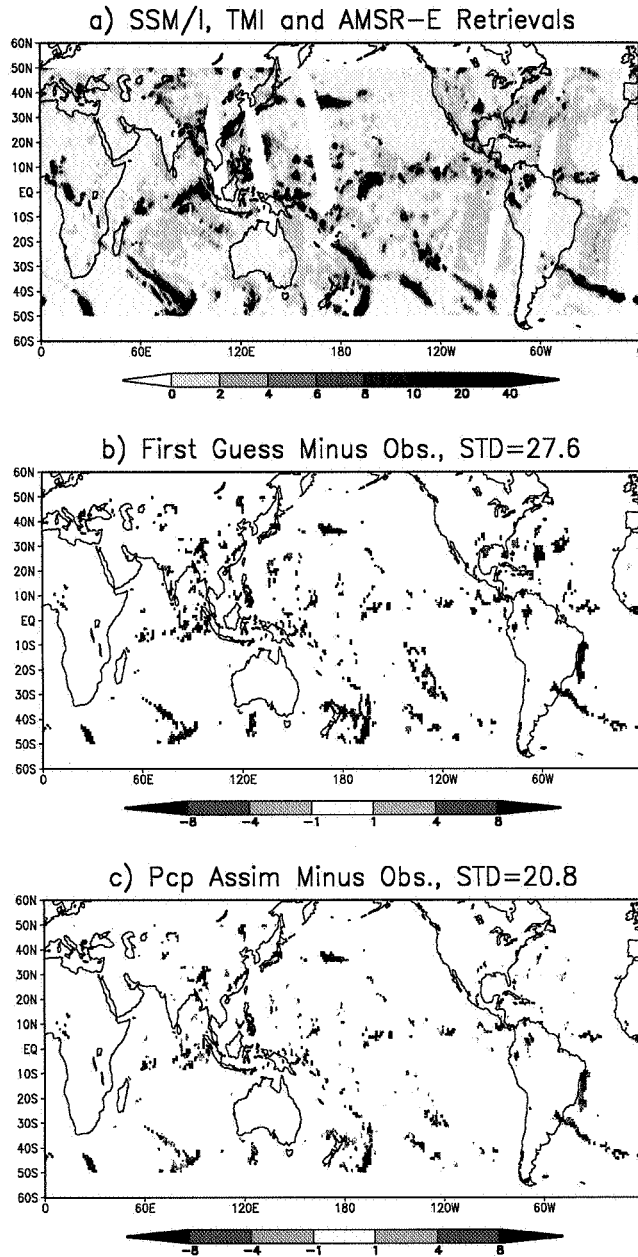


Figure 1: (a) The 6-h averaged microwave rainfall retrievals (mm/day) from TRMM TMI, DMSP F13, F14, and F15 SSM/I, and EOS AQUA AMSR-E centered at 0600 UTC on 1 July 2002; (b) Rainfall difference between the microwave rainfall observation and the column model first guess sampled at satellite ground tracks; (c) Rainfall difference between the microwave rainfall observation and the column model optimized rainfall sampled at satellite ground tracks.

Monthly-mean precipitation (mm/day, July 2002)

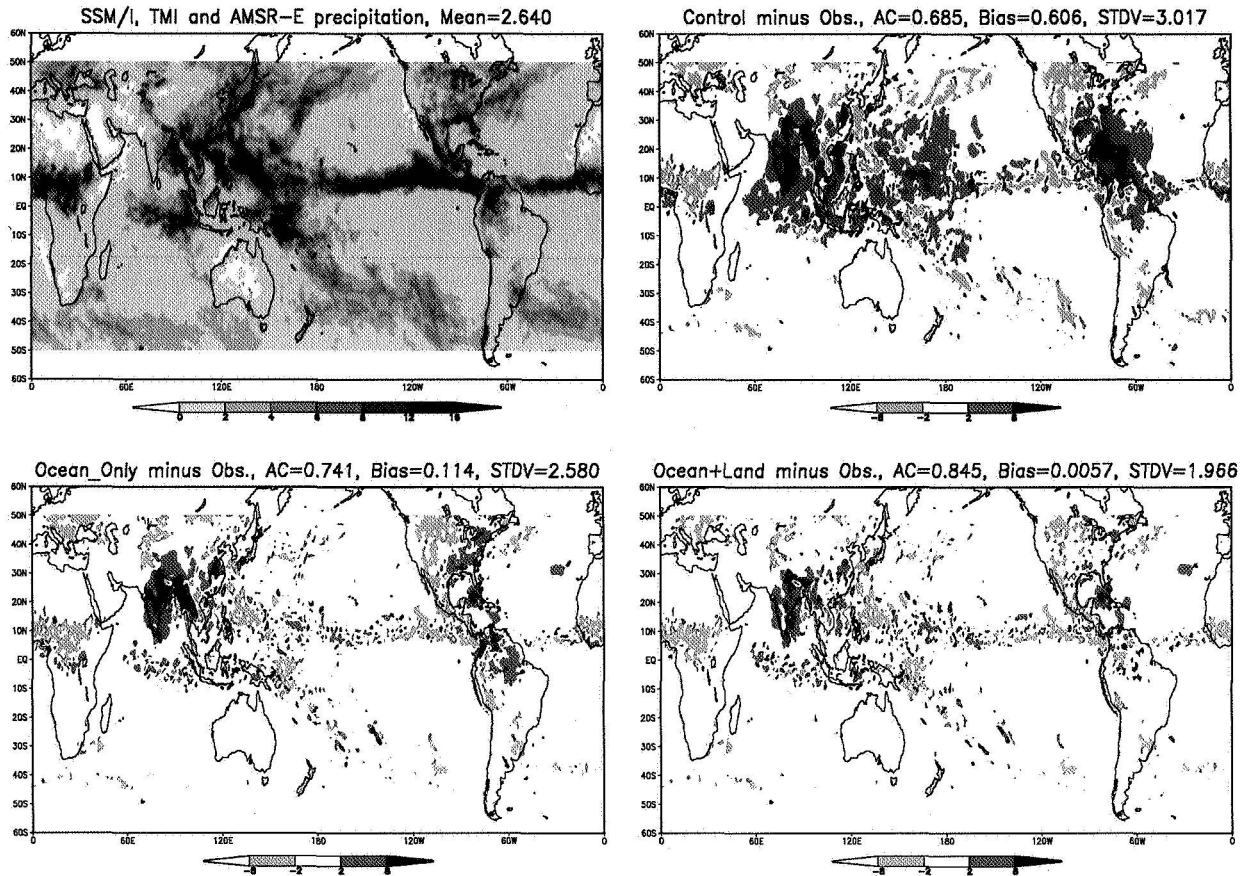


Figure 2: (a) Time-mean microwave rainfall retrievals for July 2002; (b) Difference between satellite rainfall estimates and precipitation from the control sampled at satellite observations; (c) Same as (b) but for the Ocean_only experiment; (d) same as (b) but for the Ocean+Land experiment. Also shown are the computed spatial anomaly correlation (AC), bias, and error standard deviation.

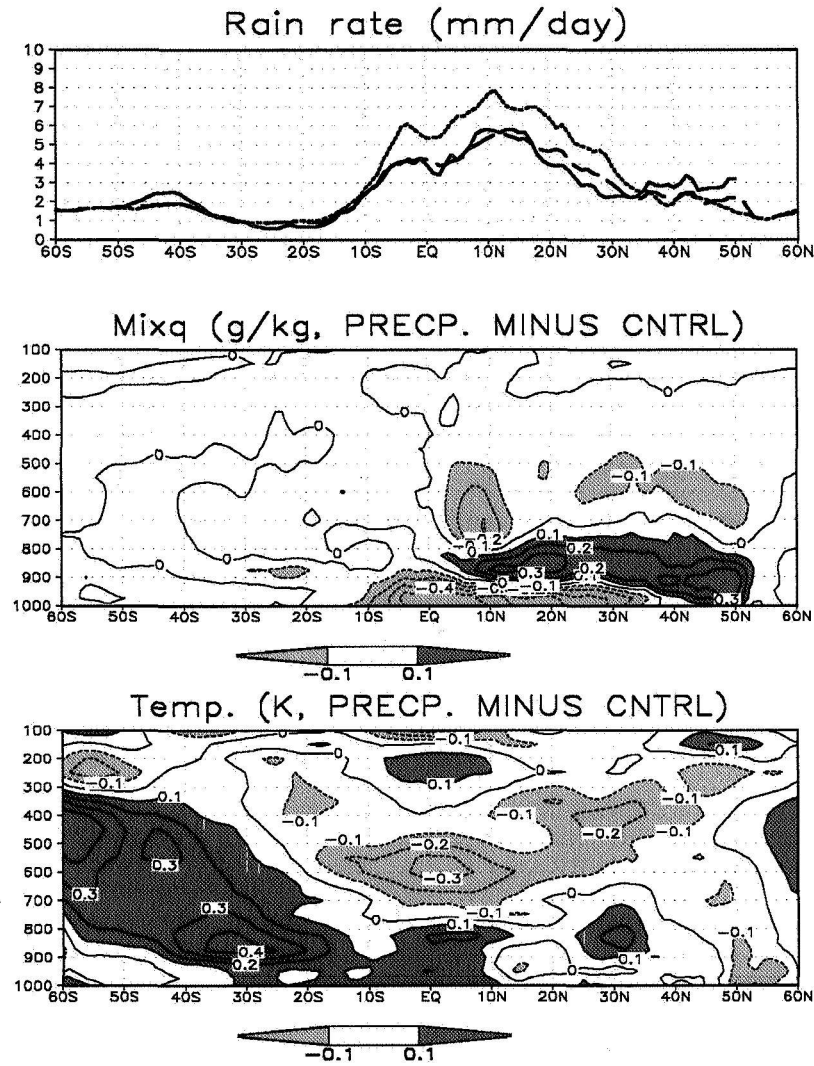


Figure 3: (a) Zonal mean rainrates (mm/day) from satellite rainfall retrievals (solid line), the control (dotted line) and the rainfall-assimilation (dashed line) runs for July 2002; (b) Zonal mean difference of mixing ratio (g/kg) between the rainfall-assimilation and the control runs; (c) Zonal mean difference of temperature (K) between the rainfall-assimilation and the control runs.

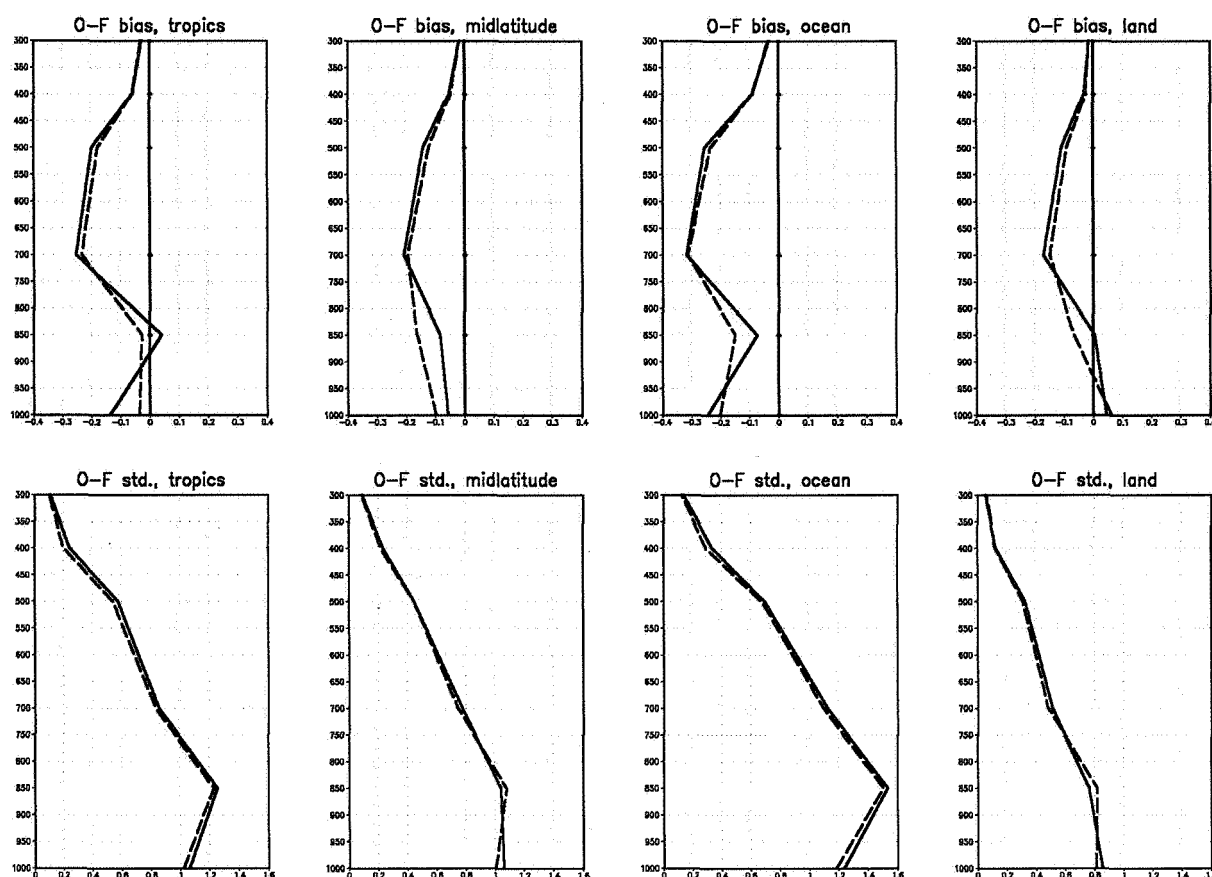


Figure 4: Mixing ratio O – F residuals (bias and error standard deviation) against rawinsonde data over the Tropics and extra-tropics, ocean and land (50°S to 50°N, July 2002): control (solid line) and Ocean+Land (dashed line).

Monthly-mean TOA Longwave Flux (W/m^2 , July 2002)

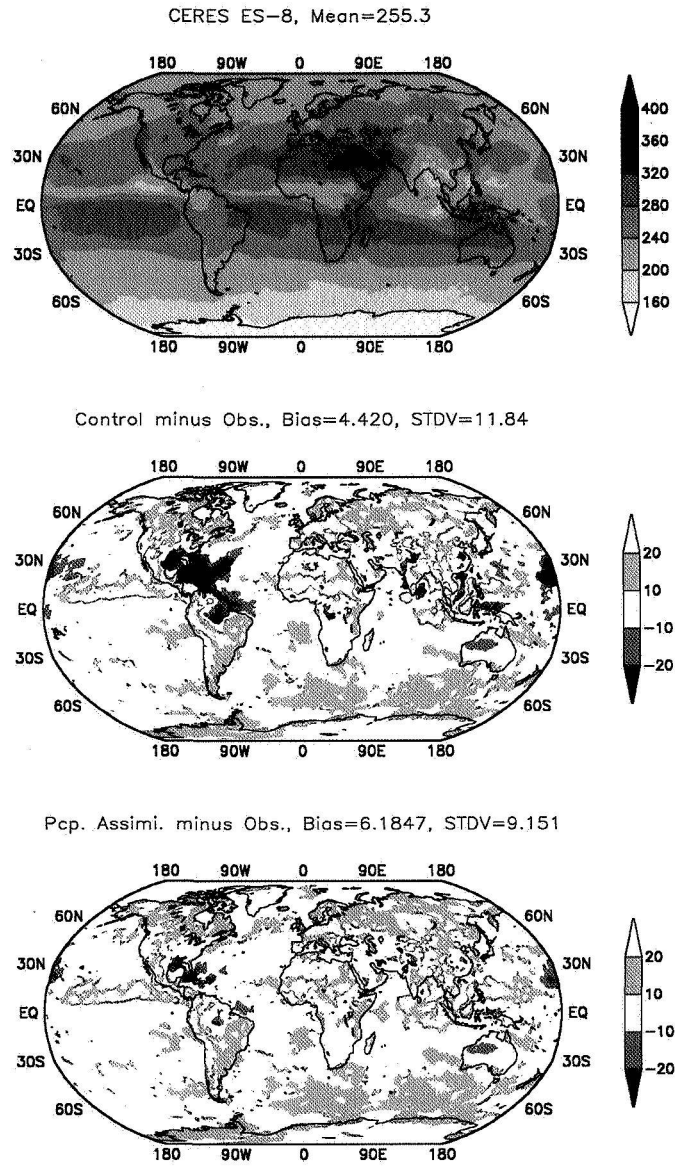


Figure 5: (a) Observed monthly-mean TOA longwave flux (W m^{-2}) from CERES ES-8 for July 2002; (b) Difference of July-mean longwave flux between the control run and the observed; (c) Difference of July-mean longwave flux between the rainfall-assimilation run and the observed.

Monthly-mean TOA Shortwave Flux (W/m^2 , July 2002)

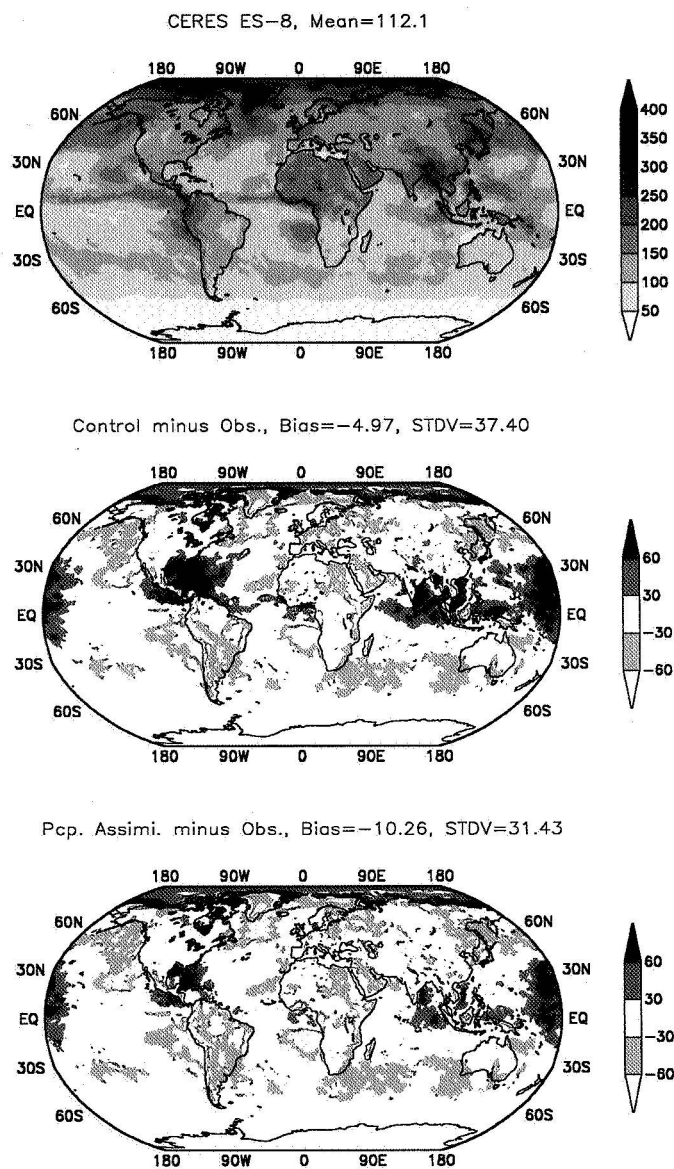


Figure 6: Same as Figure 5, but for TOA shortwave flux for July 2002.

Monthly—mean total cloud fraction (% , July 2002)

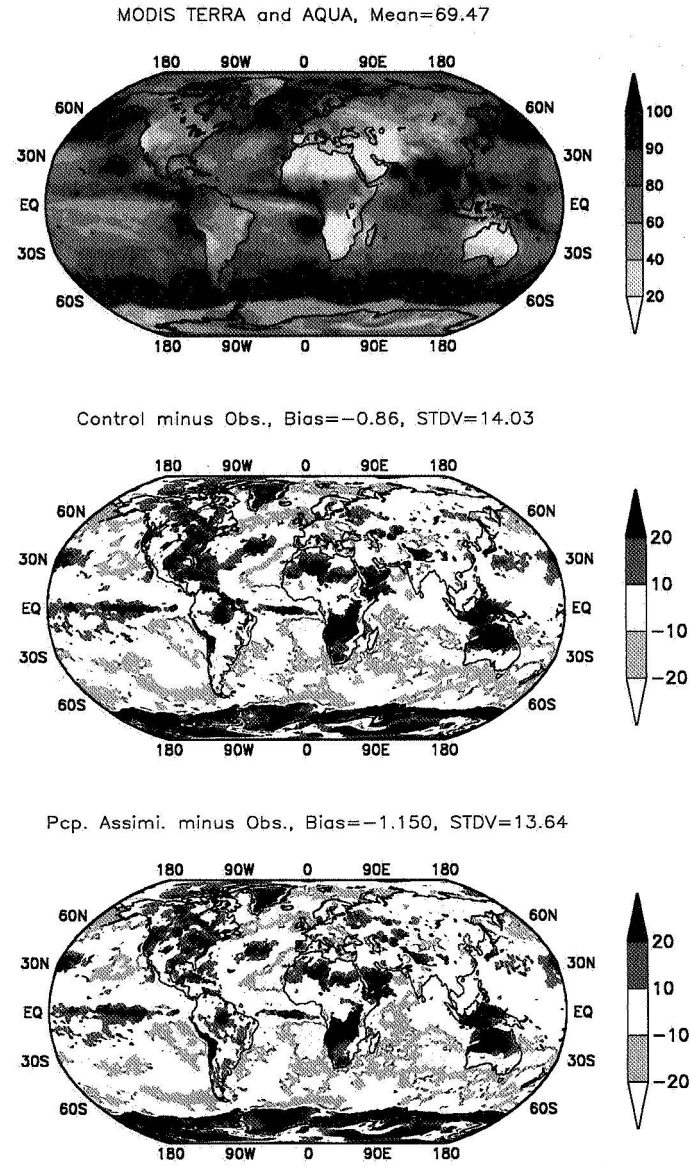


Figure 7: (a) Monthly-mean total cloud fraction (%) from MODIS, (b) Control minus observation, and (c) Ocean+Land minus observation.

One grid point in the Carribean Sea (81W, 19N, July 2002)
(the model overestimates the observed rainfall)

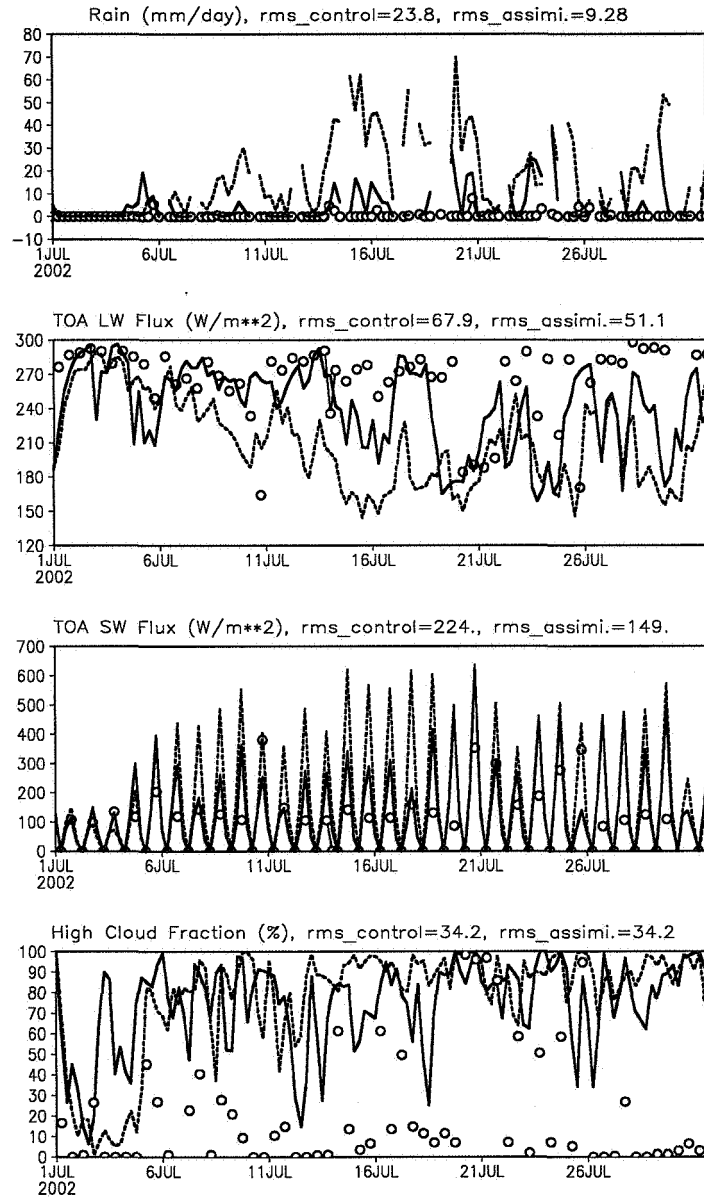


Figure 8: Time series of precipitation (mm/day), TOA longwave and shortwave fluxes ($W\ m^{-2}$), and high cloud fraction (%) for a grid point in the Carribean Sea ($81^{\circ}W$, $19^{\circ}N$) where the control run monthly-mean rainrate overestimates the observed. Observation (thin line with open circle), the control run (thick dashed line), and the rainfall-assimilation run (thick solid line).

One grid point in the tropical African Continent (21E, 8N, July 2002)
(the model underestimates the observed rainfall)

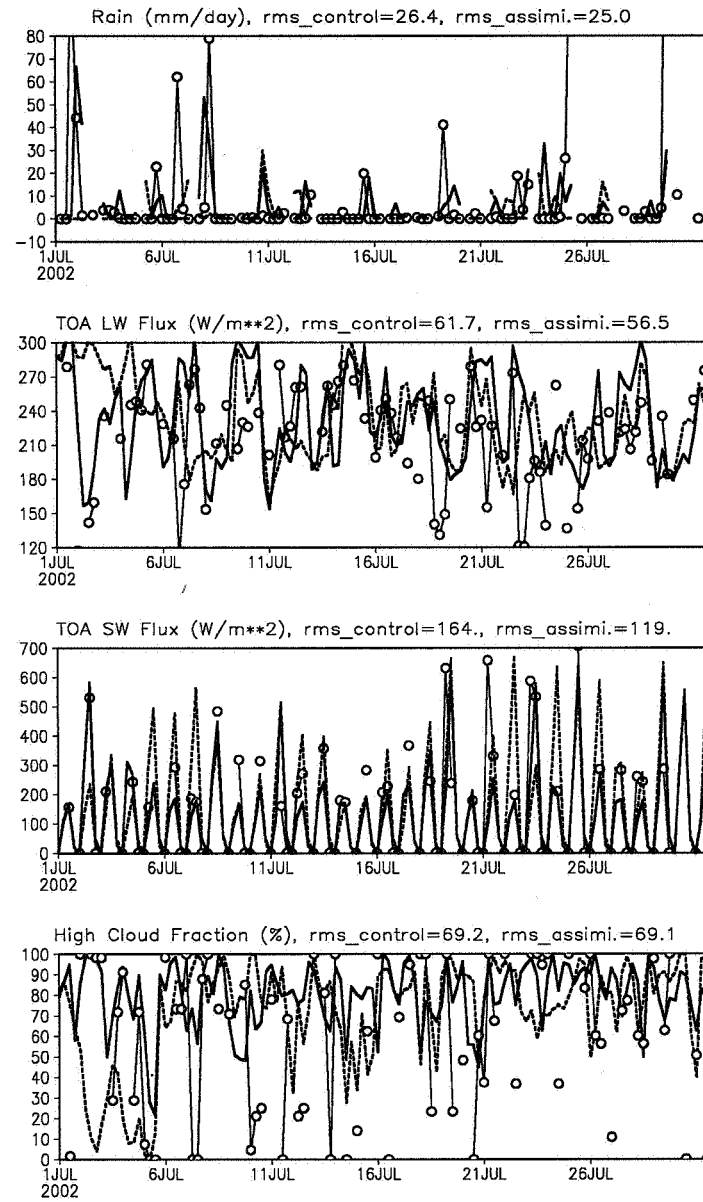


Figure 9: Same as Figure 8, except for a grid point in the tropical African Continent (21°E, 8°N) where the control run monthly-mean rainrate underestimates the observed.

One grid point in the tropical western Pacific (160E, 10N, July 2002)
(the model overestimates the observed rainfall)

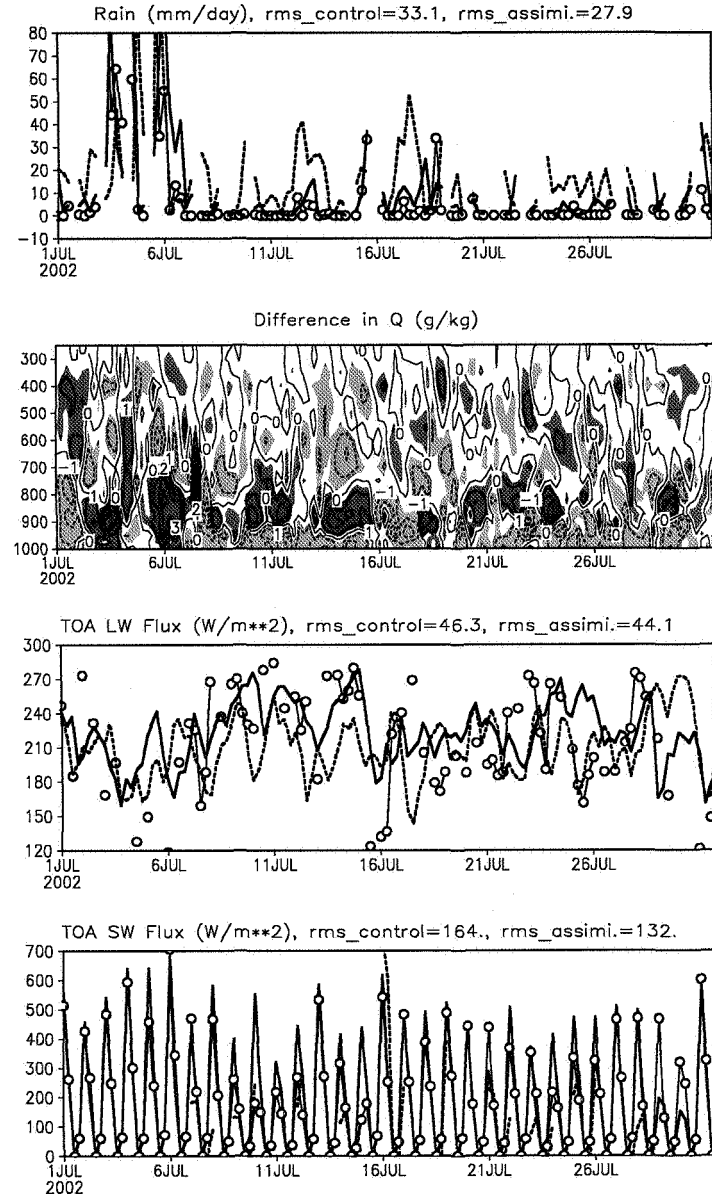
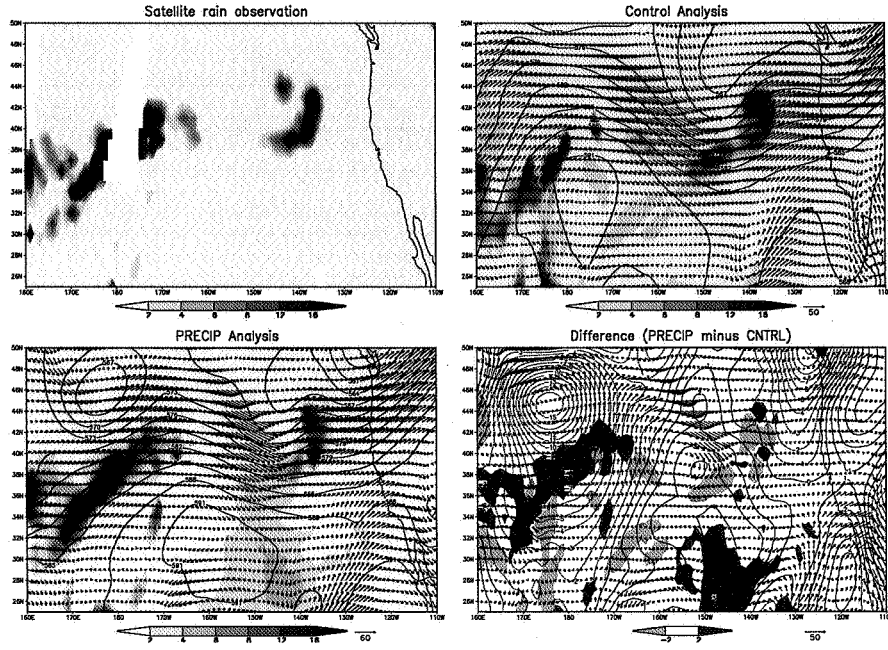
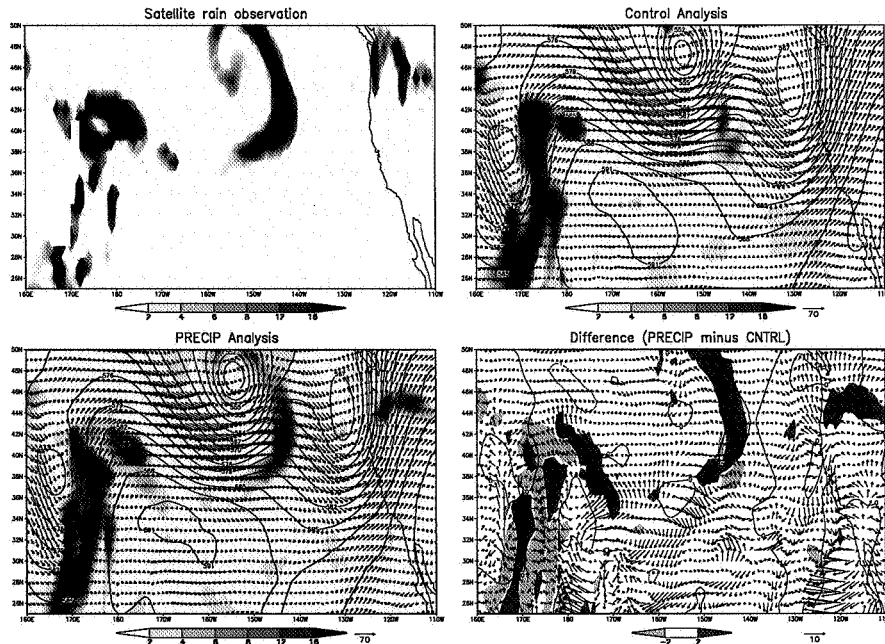


Figure 10: Time series of precipitation (mm/day), difference of vertical mixing ratio profile (g/kg), OLR (W m⁻²), and OSR (W m⁻²) between the rainfall-assimilation and the control run for a grid point in the western Pacific (160°E, 10°N) where the control run monthly-mean rainrate overestimates the observed. Observation (thin line with open circle), the control run (thick dashed line), and the rainfall-assimilation run (thick solid line).

1800 UTC, 4 July

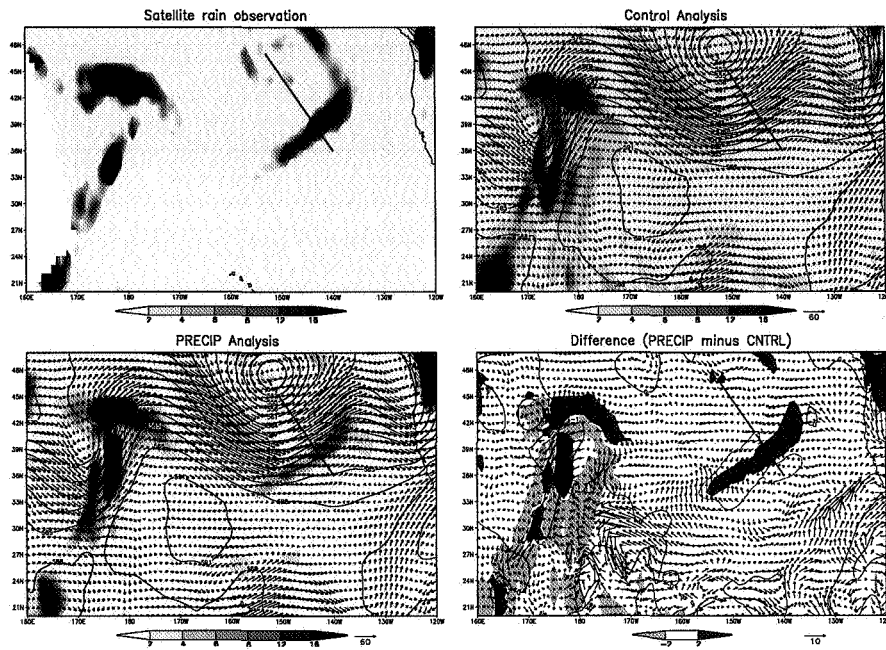


1800 UTC, 7 July

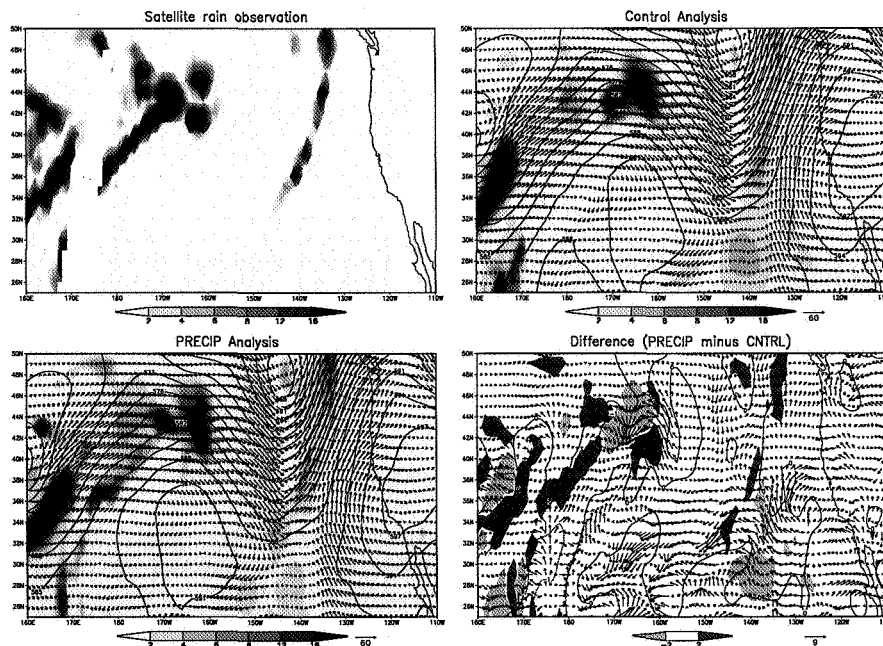


Figures 11a and 11b: (i) Satellite rainfall retrievals (mm/day); (ii) surface rainrate (mm/day), 500 hPa geopotential height (m), 200 hPa wind (m/s) from the control analysis; (iii) same as (b) but for the rainfall-assimilation analysis; (iiii) differences of surface rainrate, 500 hPa geopotential height, and 200 hPa wind between the rainfall-assimilation and the control runs.

0600 UTC, 8 July



1800 UTC, 9 July



Figures 11c and 11d: (continu

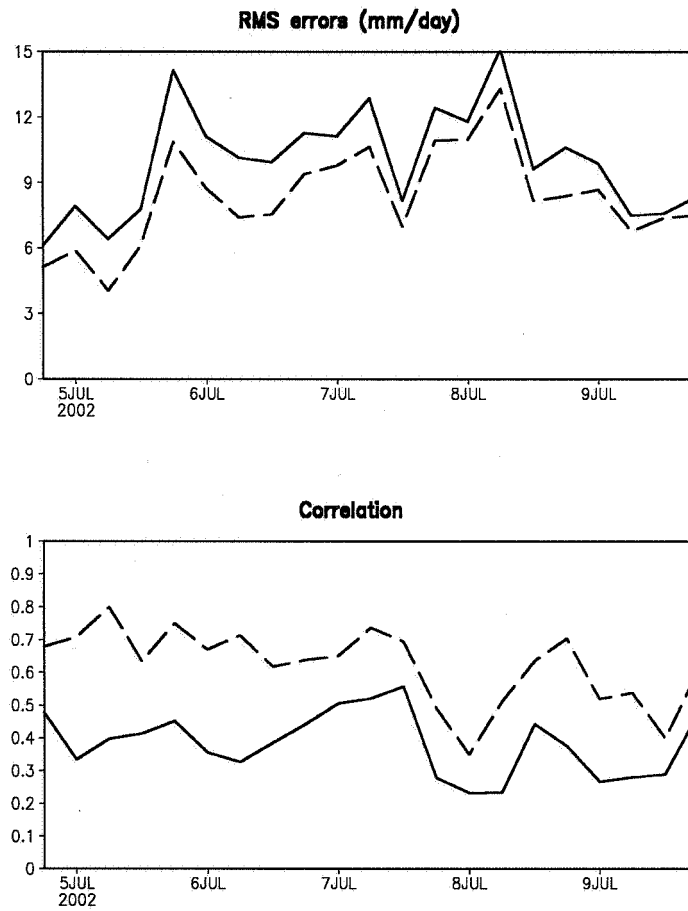


Figure 12: Rms errors and spatial correlation of 6-hourly averaged rainrate from the control (solid lines) and rainfall-assimilation (dashed lines) analyses, respectively. Combined satellite rainfall retrievals are used for verification.

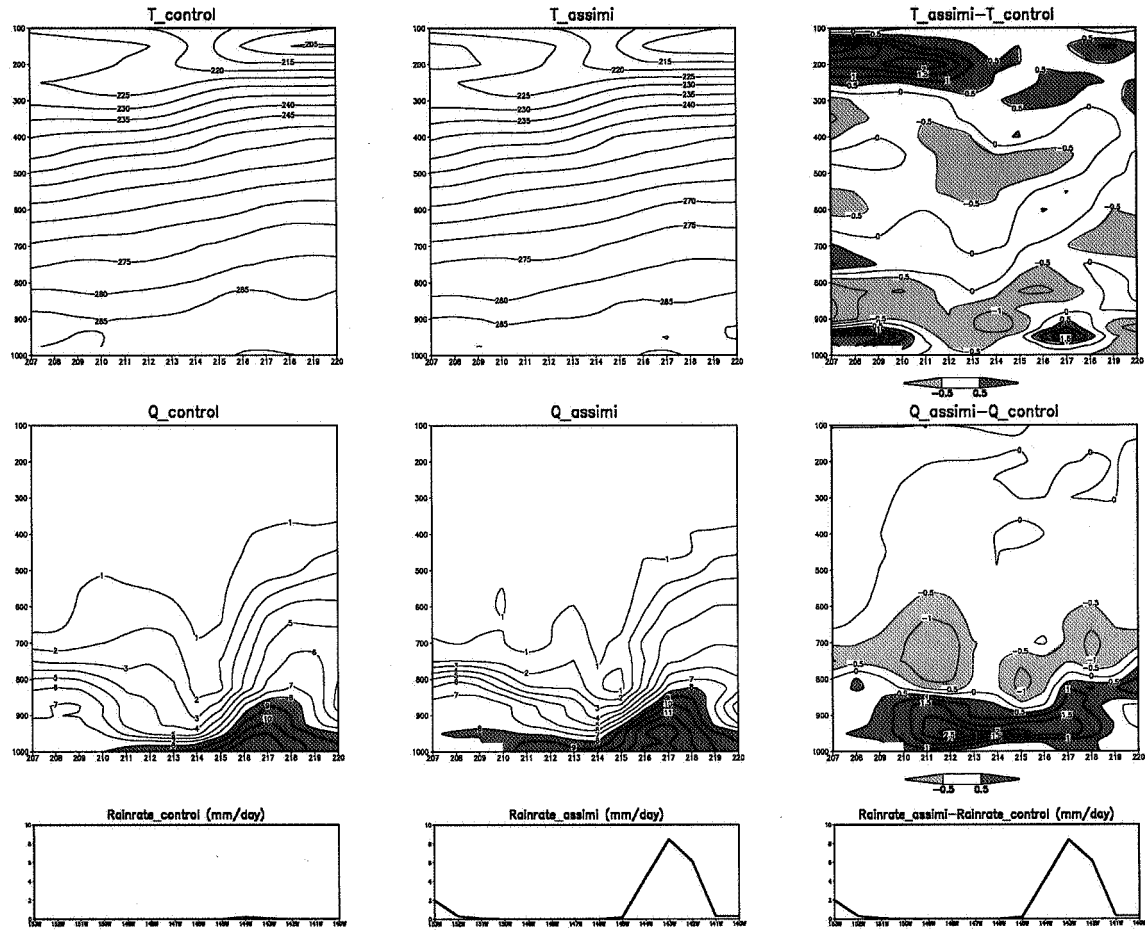


Figure 13a: Vertical cross sections of temperature (K), mixing ratio (g/kg), and their differences across the midlatitude frontal system. The contour intervals for temperatures and their differences are 10 K and 0.5 K, respectively. The contour intervals for mixing ratio and their differences are 1 g/kg and 0.5 g/kg, respectively. The mixing ratio values above 8 g/kg are darkly shaded.

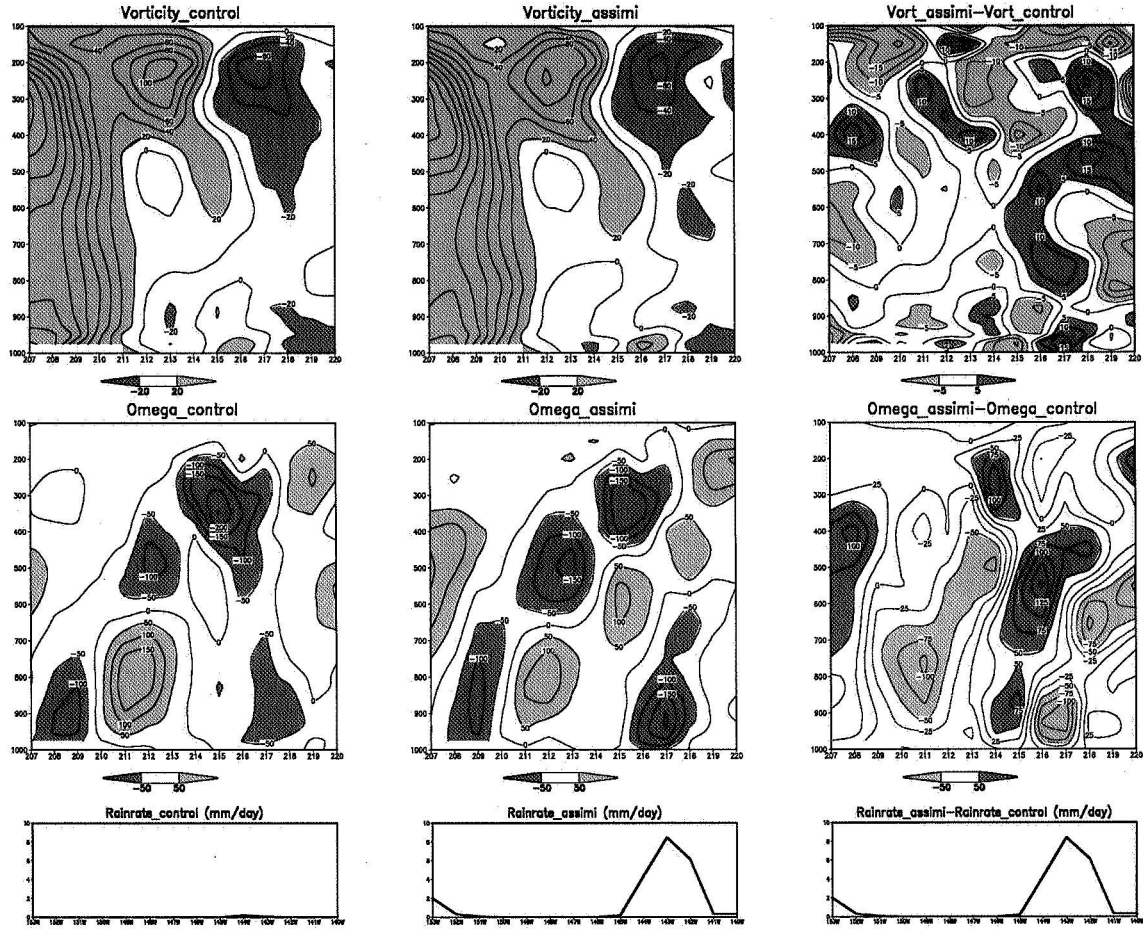


Figure 13b: Vertical cross sections of relative vorticity (10^{-6} s^{-1}), vertical motion (hPa/day), and their differences across the midlatitude frontal system. The contour intervals for vorticity and their differences are $20 \times 10^{-6} \text{ S}^{-1}$ and $5 \times 10^{-6} \text{ S}^{-1}$, respectively. The contour intervals for mixing ratio and their differences are 50 hPa/day. The vorticity and omega values above $20 \times 10^{-6} \text{ S}^{-1}$ and 50 hPa/day (below $-20 \times 10^{-6} \text{ S}^{-1}$ and -50 hPa/day) are darkly (lightly) shaded.

RMS and Correlation of a 5-day forecast
Initial condition: 0300 UTC, 06 July

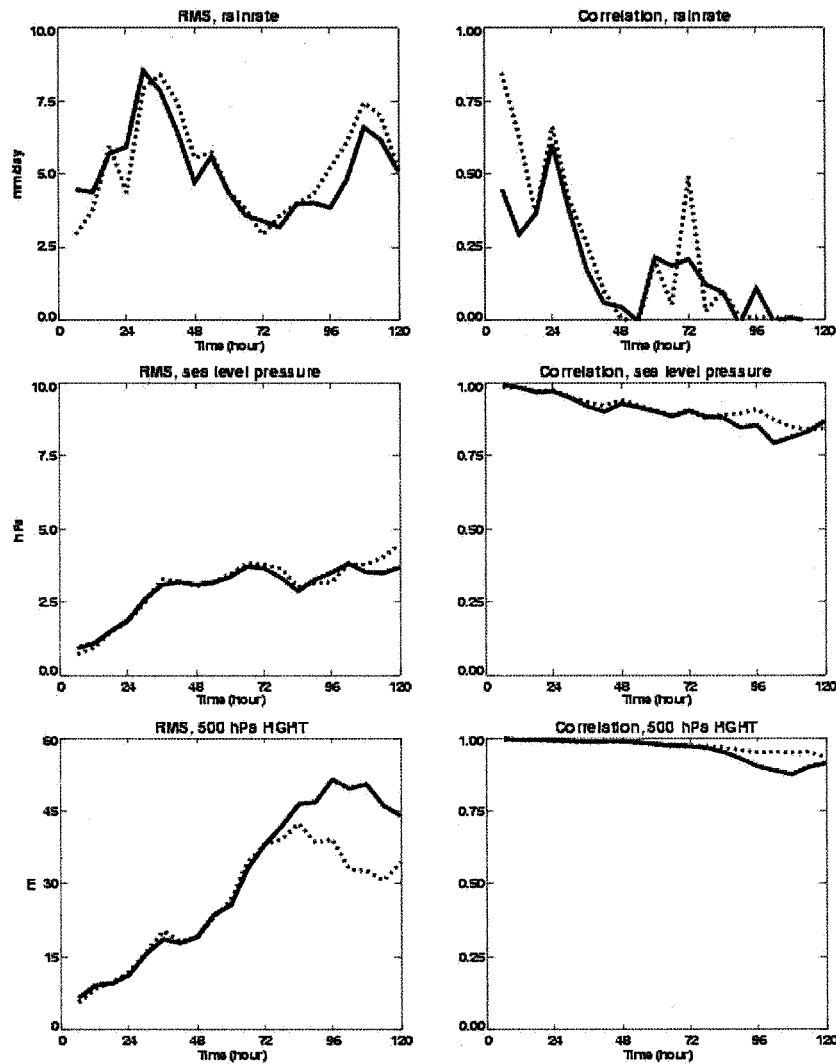


Figure 14. Rms errors and spatial correlation of 5-day forecasts of a midlatitude frontal system initialized from the control (solid lines) and rainfall-assimilation (dashed lines) analyses, respectively.